



Thermal history of Carlin-type gold deposits in Yukon (Canada) as revealed by organic matter geothermometry, clumped isotope data, fluid inclusion microthermometry, and apatite fission-track analyses

Nicolas Pinet¹ · Omid Haeri-Ardakani² · Josué Jautzy¹ · Martine M. Savard¹ · Patrick Sack³ · Patrick Mercier-Langevin¹

Received: 27 April 2022 / Accepted: 18 January 2023 / Published online: 6 February 2023
© Crown 2023

Abstract

Sediment-hosted gold deposits in central Yukon have most of the diagnostic characteristics of Carlin-type gold deposits in Nevada. This study combines organic matter geothermometry with fluid inclusion microthermometry, clumped isotope data (Δ_{47}) for late ore-stage hydrothermal calcite, and apatite fission-track analyses to constrain the thermal evolution of Carlin-type gold zones in central Yukon. The T_{max} parameter derived from pyrolysis analyses indicates that organic matter is overmature and records regional temperatures of > 150 °C. Calcite and fluorite associated with the waning stage of mineralization at ca. 74 Ma have mean fluid inclusion homogenization temperatures of 123–173 °C, with an average salinity of 4.8 wt.% NaCl equiv. These temperatures overlap values of 91–162 °C determined from calcite clumped isotope measurements and are similar to data from Carlin-type deposits in Nevada. Fluid mixing is suggested by a variation of the isotopic composition of the fluid in equilibrium with calcite, with the higher temperature end-member having higher $\delta^{18}O_{H_2O}$ values. In thermal models based on T_{max} , fluid inclusion microthermometry, clumped isotope measurements, and apatite fission-track data, a higher temperature event at approximately 220 °C is consistent with pyrobitumen reflectance measurements. This event is either related to maximum tectonic burial prior to mineralization or to the flow of acidic hydrothermal fluids early in the main ore-stage. Each analytical technique used in this study is independent of the others and records part of the thermal and chemical evolution of the Yukon Carlin-type gold deposits and their host rocks.

Keywords Carlin-type deposits · Yukon · Fluid inclusion · Clumped isotope thermometry · Organic matter reflectance · Apatite fission track

Introduction

Temperature is one of the major controls on the three components of ore genesis: metal source, transport, and deposition (Ridley 2013), and has been extensively used to

distinguish mineralization styles and to better understand ore-forming processes (Lindgren 1933). However, knowledge of the thermal framework of deposits during mineralization is often fragmentary and imprecise, relying on observations and analyses that do not yield unequivocal interpretations. This has proven to be the case for Carlin-type deposits in which Au occurs within thin (generally < 5 μm) arsenian rims on pre-ore pyrite or as sub-micrometer particles. Due to the fine-grained nature of Carlin-type Au ore, it is difficult to establish the relationships between gold and specific minerals or organic compounds that could provide temperature constraints (Cline et al. 2005). The temperature of formation for Carlin-type gold deposits in some of the major deposits in Nevada has primarily been established through the study of fluid inclusions hosted by jasperoids (fine-grained hydrothermal quartz). However, the

Editorial handling: G. Beaudoin

✉ Nicolas Pinet
Nicolas.pinet@nrcan-rncan.gc.ca

¹ Natural Resource Canada, Geological Survey of Canada, 490 Rue de La Couronne, Québec, QC G1K 9A9, Canada

² Natural Resource Canada, Geological Survey of Canada, 3303 33 Sreet NW, Calgary AB T2L 2A7, Canada

³ Yukon Geological Survey, 91807 Alaska Highway, Whitehorse, YK Y1A 5B7, Canada

temperature of hydrothermal fluids is poorly constrained for sediment-hosted gold deposits in central Yukon, which have characteristics of Carlin-type deposits (Pinet et al. 2022a). Bridging this knowledge gap should contribute to improve genetic models and document the variability within the broad spectrum of Carlin-type deposits.

Fluid inclusion microthermometry provides the most direct and, in some cases, the most accurate technique for estimating temperature of mineralization (Wilkinson 2001; Fall and Bodnar 2018). The technique is well established but can present challenges such as interpreting the potential significance of a spread in homogenization temperatures (T_h). An alternative is provided by clumped isotope thermometry, which is based on the temperature dependence of the abundance of bonds between two rare heavy isotopes (^{13}C and ^{18}O) in calcite (Eiler 2013). The direct determination of temperature from calcite clumped isotopes is a significant advantage compared to interpretations based on calcite/water O-isotope equilibrium, because temperature is calculated from a single carbonate phase (Eiler 2007). Methods based on the maturation of organic matter, such as the T_{max} parameter, which is derived from pyrolysis analyses, and organic matter reflectance, are frequently used in petroleum geology (Tissot and Welte 1984), but their application to ore deposits is less common mainly due to the relatively low temperature range over which they can be precisely applied (except for Raman spectroscopy; Beyssac et al. 2002). Moreover, an additional limiting factor is that organic matter paleothermometers only characterize the maximum temperature experienced by a sample (Hartkopf-Fröder et al. 2015), which may have been reached before, during, or after mineralization. Interpretation of low-temperature thermochronology results can also provide insights on thermal evolution at temperatures below ~ 230 °C (zircon fission-track, ZFT), ~ 120 °C (apatite fission-track, AFT), and ~ 70 °C (apatite U–Th/He). As ZFT, AFT, and U–Th/He ages rarely correspond to the age of a thermal event, modeling is required to exploit the full potential of these methods (Ketcham 2005; Malusà and Fitzgerald 2018).

The aim of this study is to investigate the fluid source(s) and formation temperature of late-ore stage hydrothermal minerals (calcite and fluorite) in the Carlin-type gold deposits in Yukon. This is accomplished using clumped isotope (Δ_{47}) and fluid inclusion microthermometric data supported by published U–Pb LA–ICP–MS calcite dating of late ore-stage hydrothermal calcite veins (Pinet et al. 2022b). Organic matter maturation data and apatite fission-track analyses make it possible to integrate temperature estimates of late ore-stage hydrothermal fluids into broader spatial and temporal frameworks. This study also provides the opportunity to discuss the merits of each method to estimate temperature.

Carlin-type mineralization in Yukon

Sediment-hosted gold deposits in the Rackla belt of central Yukon (Canada) were discovered in 2010 and have been the focus of several recent studies including a review on the regional to prospect scales (Tucker 2015; Steiner et al. 2018; Pinet et al. 2020a, 2022a), detailed descriptions of mineralized zones (Tucker 2015; Beaton 2015; Pinet and Sack 2019; Pinet et al. 2020b, 2022a), whole rock and stable isotope geochemistry (Tucker 2015; Beaton 2015; Steiner and Hickey 2019; Pinet et al. 2022a; Steiner et al. 2022), U–Pb dating of late ore-stage hydrothermal calcite (Pinet et al. 2022b), and a detailed characterization of both organic matter (Pinet et al. 2022c) and gold-bearing pyrite (Sack et al. 2019).

Gold deposits in the Rackla belt share most of the diagnostic features of Carlin-type Au mineralization in Nevada (Table 1) and are among the few examples of Carlin-type Au mineralization documented outside the south-western USA (Arehart et al. 2013; Tucker et al. 2018; Pinet et al. 2022a). Main characteristics of Yukon's deposits are summarized in Table 1, and only a brief summary is provided below. These deposits are located within paraautochthonous strata deposited on the North American continental margin east of the Tintina Fault (Fig. 1A). The Rackla belt marks the boundary between the Ogilvie Platform and the Selwyn Basin, with the latter representing a region of deep water off-shelf sedimentation that persisted from the Neoproterozoic to the Middle Devonian (Fig. 1B; Gabrielse 1967; Gordey and Anderson 1993). Gold mineralization is mainly hosted by Neoproterozoic limestone (with few mineralized intervals in siltstone) deposited in slope to base of slope settings (Nadaleen and Gametrail formations belonging to the Windermere Supergroup; Moynihan et al. 2019) and in mid-Paleozoic calcareous siltstones. In the Conrad and Sunrise/Osiris/Ibis deposits, hosted by Neoproterozoic rocks, (Fig. 1C), mineralized zones are roughly concordant with bedding and occur in mixed stratigraphic/structural traps (including anticlinal hinge zones) sealed by less permeable units. Mineralized zones are mainly hosted by carbonate floatstone and grainstone intervals interpreted to have formed through debris flow and in highly fractured sedimentary units. Most fractures and veins predate mineralization, but some are syn- to late mineralization (Tucker et al. 2018; Pinet and Sack 2019; Pinet et al. 2020a, b; Steiner et al. 2022). In contrast, the Anubis mineralized zone differs from deposits hosted by Neoproterozoic rocks located to the east (Fig. 1B) by the age and lithology of the host rocks (Paleozoic siltstones) and by greater structural control on mineralization (Pinet et al. 2022a).

The paragenetic sequence includes an early stage characterized by the dissolution of carbonates (decalcification), an intermediate stage associated with gold-bearing disseminated pyrite and fine-grained quartz (silicification),

Table 1 Main characteristics of Carlin-type deposits in Nevada (summarized from Hofstra 1994; Cline et al. 2005; Muntean 2018) and Yukon. The grey fill indicates characteristics that are discussed in the current study

	Nevada	Yukon
Regional setting	Deposits occur within the rifted cratonic margin of North America along long-lived, deep-seated basement structures	Deposits occur at the boundary between the Ogilvie platform and the Selwyn Basin along the long-lived deep-seated Dawson fault
Age	42–34 Ma; > 300 Ma younger than host-rocks	~ 74 Ma; > 270 Ma younger than host-rocks
Structural style	Pre-mineralization shallowly-dipping thrust, syn- to post-mineralization normal faults	Moderately to steeply dipping faults, tight folds
Relationship with magmatism	Clear at both the regional/district and deposit scales	Absent at the district scale. Only 2 known syn-mineralization dykes at deposit scale
Host rocks	Thin bedded carbonaceous sedimentary rocks and debris flow deposits (slope setting) ± magmatic rocks	Thin bedded carbonaceous sedimentary rocks and debris flow deposits (slope setting) ± siltstone
Organic matter maturation (host rock)	Generally overmature; Au deposition generally followed thermal maturation	Overmature; Au deposition followed thermal maturation
Ore body geometry	Large spectrum of geometries controlled by shallowly-dipping sedimentary units and/or high-angle faults; deposits are commonly located in the lower plate of a preore regional thrust (impermeable barrier)	Geometry controlled by mixed stratigraphic/ structural features; deposits commonly overlie by impermeable sedimentary units or faults
Alteration style	Decalcification, silicification, argillitization	Decalcification, silicification (± argillitization)
Late ore mineral assemblage	Calcite, realgar, orpiment, fluorite ± barite, sulfosalts	Calcite, realgar, orpiment, fluorite
Gold	Au-rich rims on preexisting pyrite and disseminated < 20 µm grains	Au-rich rims on preexisting pyrite and disseminated < 10 µm grains
Pathfinder elements	Hg, Tl, As, Sb ± Te, and Cu	Hg, Tl, As, Sb
Au/Ag	0.2 – 1	< 0.25
Temperature—ore stage (quartz)	Mostly 180–240 °C	Not documented
Temperature—late ore stage	65–140 °C	123–173 °C (fluid inclusion); 91–162 °C (clumped isotope)
Salinity- late ore stage	< 6% wt % NaCl equiv	4.8% wt % NaCl equiv
Fluid mixing	Clear	Clear
	Cline and Hofstra (2000); Muntean et al. (2011); Groff (2018)	Pinet et al. (2020a) Pinet et al. (2022b); Tucker (2015) Moynihan (2016); Steiner and Hickey (2019) Tucker (2015) Tucker (2015); Beaton (2015); Pinet et al. (2022a) This study; Pinet et al. (2022c) Tucker (2015); Pinet et al. (2022a) Pinet et al. (2022a) Tucker (2015); Beaton (2015); Pinet et al. (2022a); Steiner et al. (2022) Tucker (2015) Tucker (2015); Pinet et al. (2022a) Pinet et al. (2022a) This study; Steiner et al. (2022) This study This study

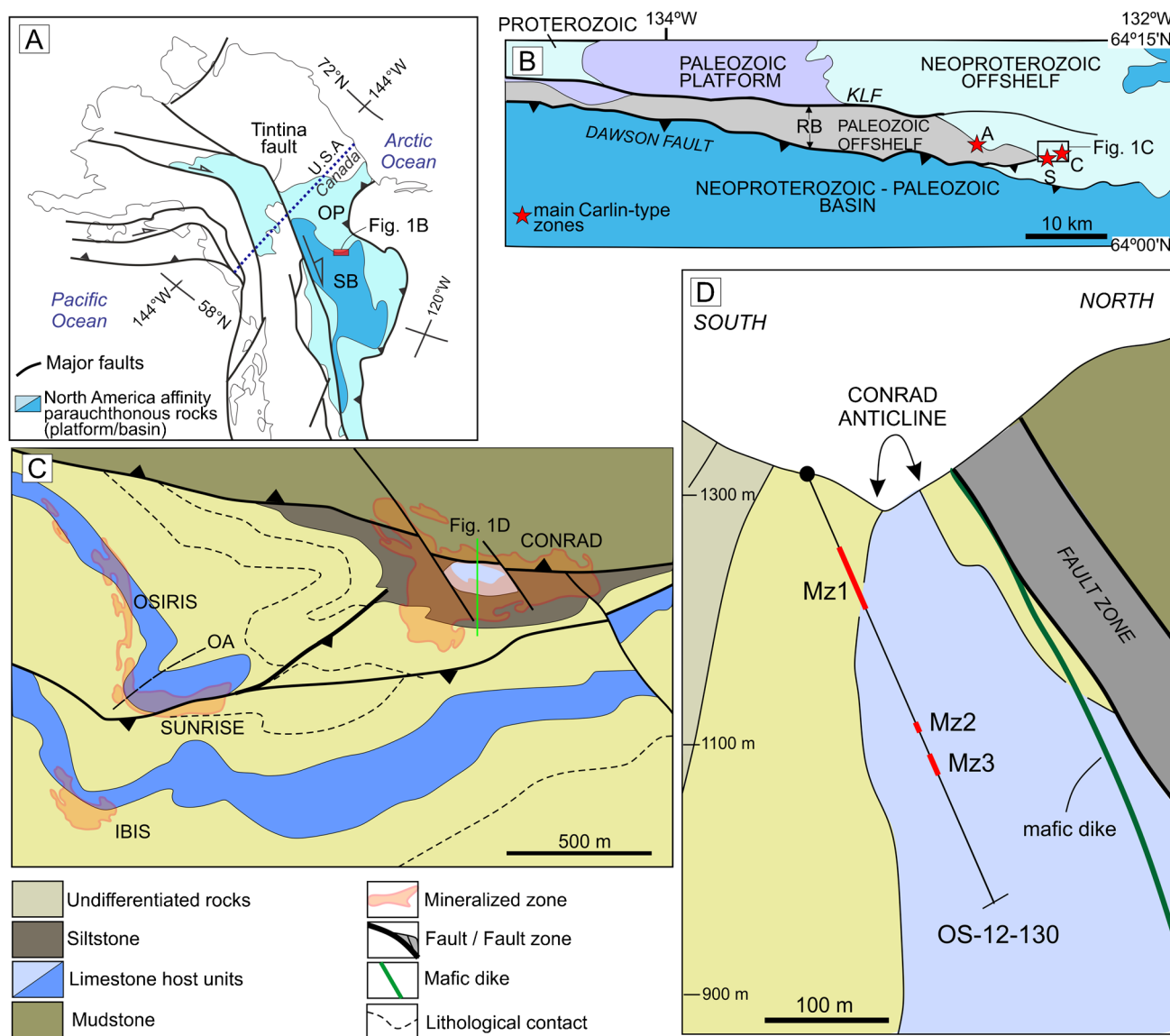


Fig. 1 Geological setting of Carlin-type deposits in Yukon. **A** Location of the study area. OP, Ogilvie platform; SB, Selwyn Basin. **B** Simplified geologic facies map of the eastern Rackla belt (after Colpron et al. 2013). KLF, Kathleen Lakes fault, RB, Rackla belt. Gold deposits: A, Anubis; C, Conrad; S, Sunrise. **C** Simplified geologic

map gold-bearing deposits hosted by Neoproterozoic rocks (modified from Atac Resources unpublished maps and Steiner et al. 2018). Mineralized area from Ristorcelli et al. (2018). **D** Cross-section of the Conrad deposit showing the location of borehole OS-12-130. Mz1, Mz2, and Mz3 refer to mineralized zones shown in Fig. 2

and a late stage characterized by the deposition of blocky calcite, realgar, orpiment, fluorite, and rare stibnite (Tucker 2015; Pinet et al. 2022a). Argillitization is local and generally difficult to document (Tucker 2015; Pinet et al. 2022a). Gold occurs within thin arsenian pyrite rims on pre-ore pyrite or as micron-scale particles in decalcified matrix material (Sack et al. 2019). Whole rock chemical analyses indicate that Au is associated with pathfinder elements such as Tl, As, Hg, and Sb, and that base metal and Ag contents are low (Tucker 2015; Beaton 2015; Pinet et al. 2022a). The timing of mineralization is ca. 74 Ma based on the combination of U–Pb dating of zircon from

a strongly altered and Au-mineralized dike (Tucker 2015) and of late-ore stage hydrothermal calcite associated with realgar (Pinet et al. 2022b).

Sample selection

Samples for pyrolysis and reflectance analyses

The data initially generated to determine the maximum temperature experienced by the samples consists of 34 programmed pyrolysis (Rock-Eval 6TM and HAWK) analyses

including 5 duplicates) corresponding to surface samples outside mineral deposits ($n = 5$) and to representative core samples from the Conrad ($n = 5$ from 3 boreholes) and Osiris/Sunrise ($n = 16$ from 2 boreholes) deposits and from the Anubis mineralized zone ($n = 8$ from 2 boreholes). Two samples among those with the highest total organic carbon (TOC) content (1.36 and 1.31 wt.%) were selected for organic matter characterization and random reflectance measurements. Sample RKA-17–27 from the Osiris/Sunrise deposit is located approximately 55 m from a mineralized interval. Sample RKA-17–70 from the Anubis zone is located within a mineralized interval yielding 8.91 g/t Au over 3.05 m (unpublished ATAC Resources database).

Subsequently, a 374-m-long borehole (OS-12–130; Fig. 1D) representative of the Conrad deposit was selected for a detailed study, with 98 HAWK pyrolysis analyses (including 7 duplicates) and reflectance measurements on 12 samples from low- and high-grade gold zones. The core from this borehole is stored at the Yukon Geological Survey (YGS) core facility in Whitehorse. The main characteristics of mineralized intervals and host rocks in borehole OS-12–130 are summarized in Fig. 2. Criteria used to pick samples for both programmed pyrolysis and reflectance analyses include fine grain size (shale to silt) and dark color (medium/dark grey to black).

A detailed description of the types of organic matter in the studied samples is presented in Pinet et al. (2022c), and salient points follow. Pyrobitumen is either disseminated in the rock, fills irregularly shaped pores (1–50 μm) and fractures, or is concentrated along stylolites (Pinet et al. 2022c). Pore-filling (\pm fracture-filling) pyrobitumen is predominant and has resulted from the thermal cracking of liquid hydrocarbon emplaced before thermal maximum and subsequently transformed to pyrobitumen through thermal cracking. In the organic-rich shale intervals, pyrobitumen is indigenous and occurs as thin laminae with shapes that resemble precursor algae transformed to pyrobitumen, or is disseminated in the shale matrix.

Samples for fluid inclusions and clumped isotope analyses

Due to the fine-grained nature of quartz associated with gold in main ore-stage mineralization (jasperoid of Lovering 1972), fluid inclusions suitable for microthermometry were not identified in any samples from the Rackla deposits. However, fluid inclusions suitable for microthermometric analysis are hosted by late ore-stage hydrothermal calcite and fluorite.

Thirteen calcite samples from the Conrad deposit ($n = 7$), Osiris/Sunrise deposits ($n = 5$), and the Anubis mineralized zone ($n = 1$) were selected from drill cores for either fluid

inclusion analysis ($n = 5$), clumped isotope measurements ($n = 5$), or both ($n = 3$). The location and main characteristics of these samples are summarized in ESM1, Table S1. All samples were selected based on their location within or proximal (< 10 m true distance) to Au-rich intervals and the presence of realgar (ESM1, Table S1). Realgar (\pm orpiment and fluorite) is spatially associated with Au-bearing intervals (Pinet and Sack 2019; Pinet et al. 2020b) and is part of the late ore-stage mineral assemblage (calcite-realgar \pm orpiment, \pm fluorite; Tucker et al. 2018; Pinet et al. 2022a, b). Cathodoluminescence (CL) imaging indicates that blocky calcite has a largely uniform orange luminescence, excluding samples RKA-17–88, RKA-17–92, and RKA-18–21 that also include dull-brown zones. Occasional brighter orange microfractures are present in some samples (ESM1, Table S1). To avoid mixing of different phases, sub-sampling for clumped isotope analyses was performed using a micro-drill in calcite zones showing homogeneous CL responses.

Samples for apatite fission-track (AFT) analyses

Fission-track analyses were conducted on samples located 0.9 and 4.3 km from Carlin-type gold-deposits, north of the Nadaleen Fault (Fig. 1). These samples were part of a regional dataset collected by the Yukon Geological Survey (Pinet and Brake 2018).

Analytical methods

Rock-Eval and HAWK programmed pyrolysis

A total of 132 bulk samples were analyzed through programmed temperature heating by Rock-Eval 6TM ($n = 6$) and HAWK ($n = 126$) pyrolysis to document the TOC content and the maturation level (Lafargue et al. 1998). Rock-Eval 6TM and HAWK programmed pyrolysis consists of programmed heating of a small amount of powdered rock (~ 70 mg) to determine the quantity of free hydrocarbons present in the sample (S1 peak) and the amount of hydrocarbons and oxygen-containing compounds (CO_2) that are produced during the thermal cracking of the insoluble organic matter (kerogen) in a sample (S2 and S3 CO_2 peaks respectively). The pyrolysis stage, conducted in an N_2 environment, begins with a 3-min iso-temperature step at 300 $^\circ\text{C}$ to release free hydrocarbons in the samples (S1, mg HC/g rock). Then, the temperature is increased at a rate of 25 $^\circ\text{C}/\text{min}$ up to 650 $^\circ\text{C}$. This results in thermal cracking and the release of hydrocarbons and the oxygen contained in pyrolyzable kerogen (S2 in mg HC/g rock and S3 in mg CO_2/g rock). Samples are then automatically transferred to the oxidation oven and heated from 300 to 850 $^\circ\text{C}$ with a heating rate of 20 $^\circ\text{C}/\text{min}$ to measure

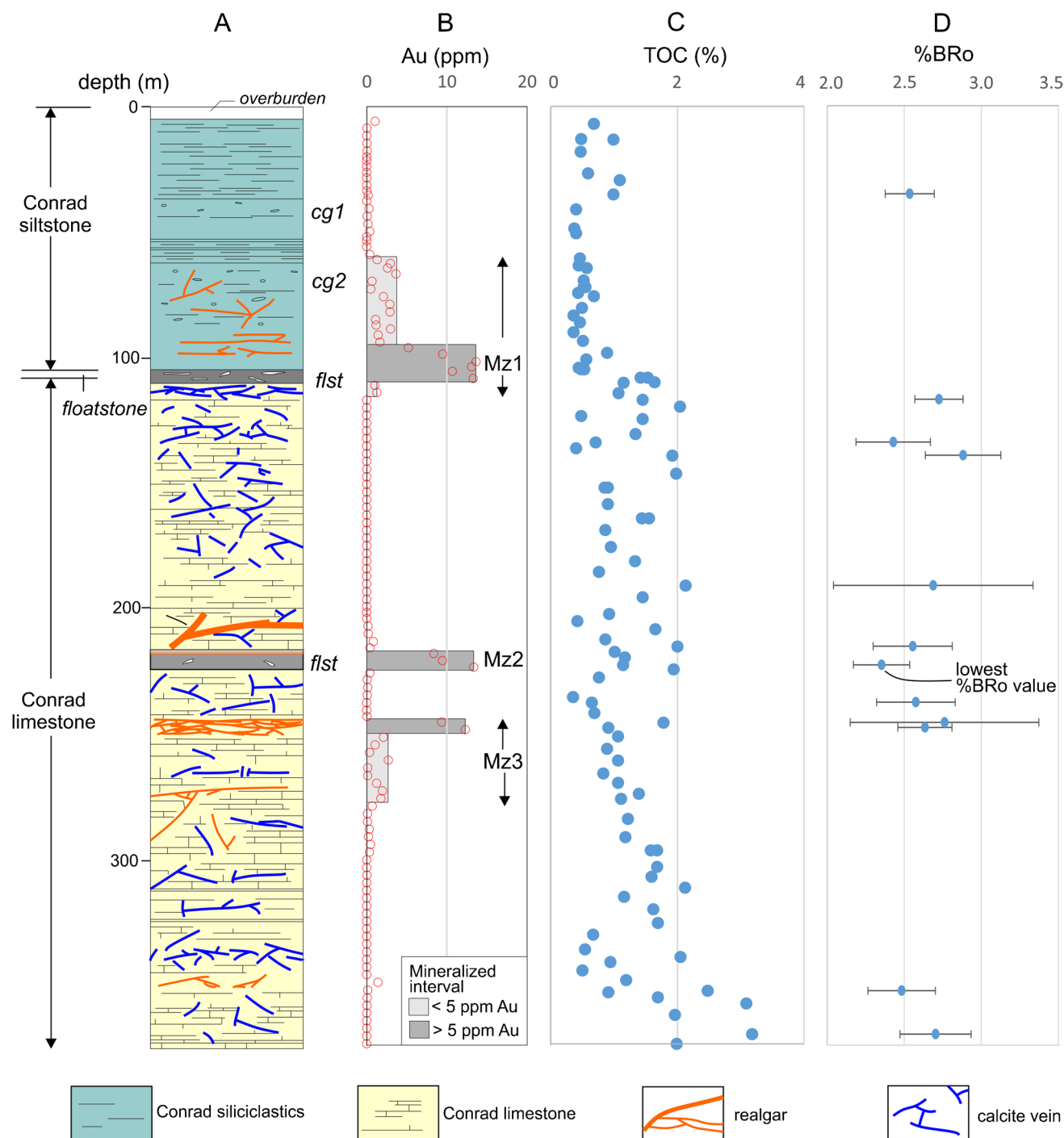


Fig. 2 Lithological and main geochemical characteristics of borehole OS-12–130. **A** Lithological column. Note the variable realgar content and occurrence of float stone intervals (flst) including one at the contact between the Conrad siliciclastics and the Conrad limestone. cg1 and cg2, conglomerate intervals. **B** Au content (from

ATAC Resources database). Mz1, Mz2, and Mz3 are the three mineralized intervals. **C** Total organic content of selected samples. Note the relatively high (> 1 wt.%) TOC values in high-grade mineralized intervals. **D** Pyrobitumen reflectance (BRo). Note that the lowest BRo value corresponds to a sample within the mineralized interval Mz2

the residual inert organic carbon (S4, mg CO₂/g rock and residual carbon, RC, wt.%) and a portion of the mineral carbon (MinC, wt.%). Total organic carbon (TOC, wt.%) is quantified as the sum of the total quantity

of organic matter released during pyrolysis (pyrolyzable carbon, PC, wt.%) and the oxidation step (RC, wt. %). The oxygen index (OI) is calculated by normalizing the quantity of pyrolyzable CO₂ (S3) to total organic carbon

(S3/TOC × 100) and is proportional to the elemental O/C ratio of the kerogen. The hydrogen index (HI) corresponds to the ratio S2/TOC × 100 and is proportional to H/C (Lafargue et al. 1998).

During programmed pyrolysis, the thermal cracking of kerogen (S2 peak) reaches a maximum at temperature T_{max} (°C), which is a commonly used thermal indicator. The T_{max} value becomes erratic below a certain level of maturation (~ 1.5% vitrinite reflectance, R_o), because the kerogen has lost almost all generative potential and the S2 peak is too small to determine an accurate T_{max}. Therefore, in overmature samples with low S2, the T_{max} cannot be used as a reliable thermal maturity proxy.

Pyrobitumen reflectance

Pyrobitumen reflectance (% BRo) analyses were conducted on 14 polished blocks with a cold-setting epoxy-resin mixture. Measurements were carried out under oil immersion following the Standard Test Method D7708 from the American Society for Testing and Material (ASTM 2014). The standard reference used for reflectance measurement was yttrium–aluminum–garnet with a standard reflectance of 0.906% under oil immersion.

Fluid inclusion measurements

Eight doubly polished 100-mm-thick wafers of calcite were prepared for fluid inclusion petrography and microthermometry (ESM1, Table S1). Samples were cut using a liquid-cooled diamond rotary saw to avoid the re-equilibration of fluid inclusions (Goldstein 2003).

Fluid inclusion microthermometric measurements were carried out using a Linkam THMG 600 heating-freezing stage at the Geological Survey of Canada, Calgary. Calibration with precision of ± 1 °C at 375 °C and ± 0.2 °C at – 56.6 °C was conducted using synthetic H₂O and CO₂ fluid inclusion standards. Heating experiments were completed prior to conducting cooling experiments to reduce the risk of stretching or decrepitating the fluid inclusions. To avoid fluid inclusion stretching during heating, we measured the T_h of all visible fluid inclusions in the same sample once. Fluid salinities were calculated from final ice melting temperatures (T_m) following Bodnar (1993).

Clumped isotope (Δ₄₇) measurements and data processing

Eight samples were analyzed at the Delta lab (Geological Survey of Canada, Quebec) using a Thermo Fisher MAT 253 equipped with seven shielded Faraday cups (*m/z* = 44–49)

and an additional half mass detector at *m/z* = 47.5 for live background monitoring. The preparation of carbonate samples was performed with an online KIEL IV carbonate device modified according to Schmid and Bernasconi (2010). Each sample was first acidified for 500 s with three drops of 104% phosphoric acid prepared following the method of Burman et al. (2005). Evolved CO₂ and H₂O were trapped continuously at LN₂ temperature followed by a 60-s pumping of non-condensable gases. The CO₂ was then released at – 100 °C and cryopumped through a Porapak trap surrounded by Ag wool, maintained at – 14 °C, into a micro-volume at LN₂ temperature. The purified CO₂ was then released into the ion source of the mass spectrometer through an inert capillary. Data for δ¹⁸O, δ¹³C, and δ₄₇ were acquired simultaneously using the long integration dual inlet (LIDI) method (Müller et al. 2017). Each measurement comprised 70 cycles of 10-s integrations of the unknown gas followed by a similar integration process for the working gas (δ¹³C = – 4.5‰ V-PDB, δ¹⁸O = 15.9‰ V-SMOW). Each sample was analysed at least 14 times, and standards were interspersed in a 50/50 proportion in order to achieve a precision of < 0.01‰. The data acquired for this study has been archived in the EarthChem, ClumpDB database under the following <https://doi.org/10.26022/IEDA/112497>.

Raw beam intensities were imported in Easotope (John and Bowen 2016) for calculation of the Δ₄₇. The IUPAC parameters (Brand et al. 2010) were used to correct for ¹⁷O interferences as suggested by Schauer et al. (2016) and Daëron et al. (2016). We adopted a fully carbonate-based calibration scheme using the carbonate standards (ETH1-4) developed at ETH-Zurich (Meckler et al. 2014) and used the recently accepted InterCarb values (Bernasconi et al. 2021). ETH-1 and ETH-2 were used to correct for the non-linearity effect in the ion source, whereas ETH-1, ETH-2, and ETH-3 were used to construct the empirical transfer function (ETF) for translation of the measurement to the CO₂ equilibrium scale (CDES70C). The calibration was made before and after each analysis of each unknown using a running window of 56 standards to correct for slight drift in ion source stability. Negative background corrections were performed using the pressure baseline correction (Bernasconi et al. 2013; He et al. 2012) after every 46 analyses. This was achieved by using high-voltage scans made between 5 and 25 V intensities (*m/z* = 44) in 5-V increments to produce a correction function that can be applied to the decaying intensity inherent to the LIDI method of measurement. A composite T-Δ₄₇ produced from the calibration of Jautzy et al. (2020) and recalculated using the InterCarb ETH values (Bernasconi et al. 2021) and all the calcite temperature anchors from Anderson et al. (2021) (all projected back to 70 °C using the acid reaction correction of Petersen et al. 2019) was applied to convert Δ₄₇ values into temperatures.

Apatite fission track analyses

Apatite grains for AFT dating were extracted from samples following conventional separation methods. Apatite fission track ages were determined by Apatite to Zircon Inc. from spontaneous fission track densities in individual apatite grains and relative uranium concentrations using the LA–ICP–MS method (see analytical procedure in Donelick et al. 2005). Electron microprobe micro-analysis data were collected for the same age/length grains that have undergone AFT analysis. These apatite elemental composition data provide kinetic information for use in the thermal history modeling.

Results

Rock–Eval 6TM and HAWK programed pyrolysis

Results of programed pyrolysis analysis are presented in Electronic Supplementary Material (ESM1, Table S2). The TOC content ranges from 0.25 to 3.18 wt.% with a mean value of 1.05 wt.%. Considering the high degree of maturation of these samples (see below), the original organic matter content was probably higher than that measured today (Jarvie et al. 2007) and comparable to some Phanerozoic hydrocarbon-prone basins (Tissot and Welte 1984).

All surface and core samples analyzed through programed pyrolysis have S1 (free hydrocarbon) and S2 (hydrocarbon potential/kerogen content) values close to 0 (average = 0.04 ± 0.04 mg HC/g for both S1 and S2). This indicates that there is no free hydrocarbon and hydrocarbon potential remaining, and that samples are overmature (maximum temperature experienced by the sample > 150 °C). Due to the very low S2 content, the T_{max} (i.e., thermal maturity proxy) varies from 289 to 668 °C, which is not reliable. The mean hydrogen index (HI) and oxygen index (OI) of the samples are 3.8 ± 4.0 mg HC/g TOC and 47 ± 32 mg CO₂/g TOC, respectively (ESM1, Table S2). All these values are typical of overmature samples.

Pyrobitumen reflectance

Pyrobitumen reflectance (BRo) measurements provide an indicator of the thermal maturity of the samples. A total of 12 samples from borehole OS-12–130 record mean BRo values of 2.35–2.88% (Fig. 2D; Table 2), which indicates high thermal maturity, further confirming the programed pyrolysis data indicative of overmature samples. The lowest BRo (2.35%) value corresponds to a high-grade sample (13.35 ppm Au over 2.21 m) at 224 m (Fig. 2). The average

Table 2 Pyrobitumen reflectance results (BRo). Results for the borehole OS-12–130 are shown graphically in Fig. 2

Borehole	Deposit	Depth (m)	Mean %BRo	stdev	n
OS-12–130	Conrad	35.0	2.54	0.16	30
OS-12–130	Conrad	116.7	2.73	0.16	12
OS-12–130	Conrad	133.7	2.43	0.24	118
OS-12–130	Conrad	139.0	2.88	0.25	30
OS-12–130	Conrad	190.7	2.69	0.65	111
OS-12–130	Conrad	214.9	2.56	0.26	72
OS-12–130	Conrad	222.3	2.35	0.18	40
OS-12–130	Conrad	237.2	2.58	0.26	231
OS-12–130	Conrad	245.2	2.76	0.61	78
OS-12–130	Conrad	351.9	2.48	0.22	40
OS-12–130	Conrad	369.2	2.70	0.23	110
OS-12–130	Conrad	247.2	2.63	0.18	50
OS-13–217	Sunrise	120.0	1.8	0.15	21
AN-16–10	Anubis	27.0	1.76	0.18	91

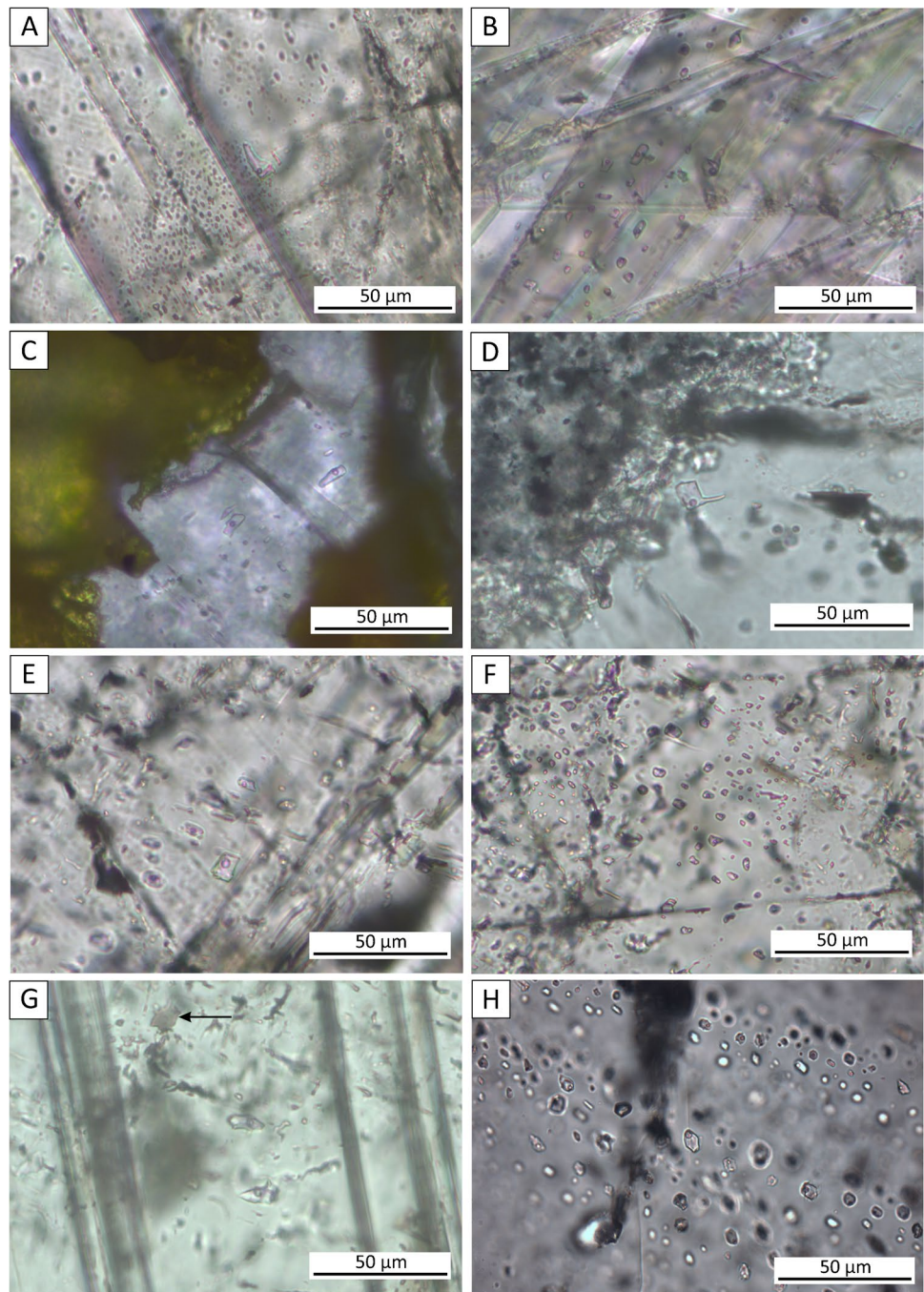
pyrobitumen reflectance (% BRo) value for all samples from borehole OS-12–130 is 2.61%, which corresponds to 2.77% equivalent vitrinite reflectance (VRo_{eqv}) using the conversion equation of Landis and Castaño (1995). A maximum paleo-temperature of ca. 220 °C is estimated based on the relationship between Ro and temperature as proposed by Barker and Pawlewicz (1994) for “slow” (regional) heating rates. Slightly higher temperature estimates would be associated with “fast” (hydrothermal) heating rates.

The mean Bro data for the samples from the Sunrise deposit (Neoproterozoic laminated pyritic shale with mainly dispersed pyrobitumen in the matrix) and from the Anubis zone (dark gray Paleozoic siltstone with pore-filling solid pyrobitumen) are $1.8 \pm 0.15\%$ and $1.76 \pm 0.18\%$, respectively (Table 2), slightly lower than for borehole OS-12–130 but still indicative of an overmature state.

Fluid inclusions

In calcite crystals, fluid inclusions occur mainly along cleavage planes (Fig. 3A and B) and crystal boundaries as random individual fluid inclusions (Fig. 3C and D) and as clouds of numerous fluid inclusions without any specific spatial relationship with calcite cleavage planes (Fig. 3E, F, and G). The similar liquid/vapor (LV) ratio of fluid inclusion assemblages suggests that fluid inclusions did not neck-down after the fluid inclusions have reached the LV curve on their retrograde path (Goldstein 2012). Most isolated inclusions do not show clear petrographic evidence for a relationship to growth of the host crystal and cannot be classified as primary or secondary using the criteria provided by Roedder (1984). For this reason, interpretation of the fluid inclusions as primary ($n = 85$), secondary ($n = 17$),

Fig. 3 Photomicrographs of fluid inclusions. All images were taken with white transmitted light, and all host minerals are calcite unless specified. **A** A solitary LV fluid inclusion along a calcite cleavage plane and clouds of very small fluid inclusions distributed in over the field of view (RKA-17–92). **B** An assemblage of LV inclusion between cleavage planes (RKA-17–105). **C** A LV small fluid inclusion assemblage hosted by pore-filling calcite within a realgar matrix (RKA-17–105). **D** A LV fluid inclusion close to the host (RKA-17–95). **E** Cloud of LV fluid inclusions. **F** Cloud of small fluid inclusions in the calcite matrix (RKA-17–99). Note that the small size of fluid inclusions made microthermometry difficult and in some cases impossible. **G** Two large LV fluid inclusions among smaller fluid inclusions between calcite cleavage planes (RKA-17–65). The black arrow highlights a single-phase gas inclusion. **H** Trails of small LV fluid inclusions in fluorite (RKA-18–06)



and pseudo-secondary ($n = 12$) was done on a part of the set of measured inclusions only ($n = 248$ in calcite), with others being classified as undetermined. Fluid inclusions in fluorite (sample 18–06) are much more abundant and occur as fluid inclusion trails (Fig. 3H). Because of lack of clear crosscutting relationships and/or clear crystal growth zonation, the identification of the origin of fluid inclusions, especially in fluorite, was not possible. Fluid inclusions are dominantly liquid vapor (LV) in both calcite and fluorite (Fig. 3), with rare one-phase vapor inclusions (Fig. 3E).

Overall, the inclusions are generally small (3–15 μm , average $\sim 5 \mu\text{m}$; Fig. 3), which made observing the last ice melting temperature very difficult and the salinity of fluids impossible to determine accurately in some cases. Under ultra-violet (UV) light, none of the fluid inclusions fluoresced, indicating that they are aqueous.

The microthermometric results are presented in Table 3. Homogenization temperature (T_h) for all calcite-hosted fluid inclusions range from 77.1 to 254 $^{\circ}\text{C}$ (Fig. 4A), and the average for all inclusions is 150.6 $^{\circ}\text{C}$. This average is close to the

Table 3 Summary of fluid inclusion microthermometry and clumped isotope results

Sample	Fluid inclusion										Clumped isotope										U–Pb Geochronology						
	T_h (°C)					Salinity (%NaCl)					$\delta^{13}C$ (‰)					$\delta^{18}O$ (‰)											
No	Mineral	n	Mean	Median	std	Min	Max	n	Mean	n	$\delta^{13}C$ (‰) VPDB	$\delta^{13}C$ (‰) SD	$\delta^{18}O$ (‰) VSMOW	$\delta^{18}O$ (‰) SD	Δ_{47} (‰) CDES	Δ_{47} (‰) SD	Δ_{47} (‰) SE	T_{sp} (°C)	+7° SE	-7° SE	$\delta^{18}O_{water}$ (‰) VSMOW ¹	$\delta^{18}O_{water}$ (‰) VSMOW ²	U–Pb (Ma)	U–Pb complexity			
Conrad deposit																											
RKA-17-65	Cal	21	123.3	119.1	15.2	96	154.6	3	4.3	14	-2.9	0.05	15.53	0.02	0.376	0.038	0.01	162	10	11	6	3.8		71.2±4.3	Simple		
RKA-17-88	Cal	8	133.5	139.7	30.4	94.2	172.2	0																NQA	Complex		
RKA-17-104																											
RKA-17-105	Cal	29	146.6	144	18.9	118.5	182	7	4.5	16	-2.72	0.03	15.61	0.03	0.397	0.036	0.009	141	8	8	4.1	-3.8		72.7±6.2	Simple		
RKA-17-108	Cal	26	123.4	110.5	30.7	86.1	167.3	0		24	-0.02	0.02	24.11	0.05	0.416	0.048	0.01	125	8	8	10.7	8.6		75.1±2.5	Simple		
RKA-18-06																											
RKA-18-06	Cal	84	172.6	168.5	30.6	85	254	17	6.9																		
RKA-18-06 Fluo																											
RKA-18-06	Fluo	10	154.4	156.5	12.6	130	174.1	3	3																		
RKA-18-37																											
RKA-18-37	Cal	14	0.1	0.22	17.60	0.25	0.455	0.028	0.008	97	5	5	1	-1										66±16	Complex		
Osiris deposit																											
RKA-17-92	Cal	25	143.4	140	21.5	110	181	8	2.6																		
RKA-17-95	Cal	46	127.6	131.1	26	71.1	178.5	0																			
RKA-17-99	Cal	7	150.5	159.8	23.9	107	175.8	0																			
RKA-18-14	Cal	18	-4.07	0.13	18.05	0.12	0.407	0.036	0.008	132	7	7	5.5	3.4													
RKA-18-24	Cal	18	-1.11	0.04	17.63	0.08	0.437	0.043	0.01	109	7	7	2.5	0.5													
Anubis mineralized zone																											
RKA-18-21	Cal	14	-0.14	0.06	23.17	0.13	0.432	0.036	0.01	113	7	8	8.4	6.4													

1 Calculated from Kim and O'Neil (1997); 2 calculated from Daëron et al. (2019)

NQA, no quantitative age estimate

mean T_h for primary (144.3°) and “undermined” (149.7°) fluid inclusions, as well as to the relatively small number of inclusions interpreted as pseudo-secondary (148.7 °C) and secondary (158.4 °C).

All samples show unimodal distribution of T_h values with two exceptions, samples RKA-17-92 and RKA-17-108 ($n=25$ and $n=26$, respectively), which exhibit a slightly bimodal distribution. The majority of samples has a similar range of T_h values, and mean temperatures between 123.3 and 150.5 °C, except for sample RKA-18-06 from the Conrad deposit that has a notably higher mean T_h value of 172.6 °C for calcite ($n=84$). However, the mean T_h value of fluid inclusion in fluorite for this sample is 154.4 °C ($n=10$), which is ~18 °C cooler than the mean T_h value for calcite. At a first glance, the microthermometry results for the Conrad deposit ($n=5$) suggest that hydrothermal fluids were hotter ($T_h=169.5$ °C) than those of the Osiris/Sunrise deposits ($n=3$, $T_h=134.7$ °C). However, this difference decreases to <3 °C if the data for sample RKA-18-06 are removed from the calculation.

The mean calculated salinities for calcite- and fluorite-hosted fluid inclusions are 5.2 ± 3 wt.% NaCl equiv. ($n=35$) and 3.0 ± 0.6 ($n=3$), respectively (Fig. 4B). Among the 11 inclusions with salinities of >6 wt.% NaCl equiv., nine are from sample RKA-18-06, which is the only sample in which inclusions in fluorite have been measured. The three highest salinity values (7.6–14.6 wt.% NaCl equiv.) were obtained for primary inclusions.

Clumped isotopes

Clumped isotope results are presented in Table 3 and Fig. 5. Samples of late ore-stage hydrothermal calcite from the Conrad and Osiris/Sunrise deposits have $\delta^{18}O_{VSMOW}$ and $\delta^{13}C_{VPD}$ values of 15.52–24.11‰ and -4.07 – -1.02 ‰, respectively. Samples RKA-17-108 (Conrad deposit) and RKA-18-21 (Anubis zone) have the highest $\delta^{18}O_{VSMOW}$ values of 24.11 and 23.17‰ (Fig. 5A), respectively. However, their $\delta^{13}C_{VPD}$ values are ~0‰ and within the range defined by other samples (Fig. 5A). With respect to geology, sample RKA-17-108 is from the highly fractured hinge zone of the Conrad anticline (Fig. 6) and was analyzed twice with similar results.

The five samples from the Conrad deposit yielded apparent temperatures (Δ_{47}) of 91 ± 5 to $162 + 10/-11$ °C with the highest temperature recorded by the two deepest samples (RKA-17-65 and RKA-17-105) and the lowest for a shallow sample (RKA-17-104) proximal to the Nadaleen Fault (Fig. 6). Decrease in yielded temperature with altitude possibly indicates the cooling of hydrothermal fluids during upward migration. Sample RKA-17-104 is the closest to a mafic dike (Fig. 6), but it does not record a thermal imprint expected to be associated with dike emplacement, further suggesting that hydrothermal calcite post-dates the

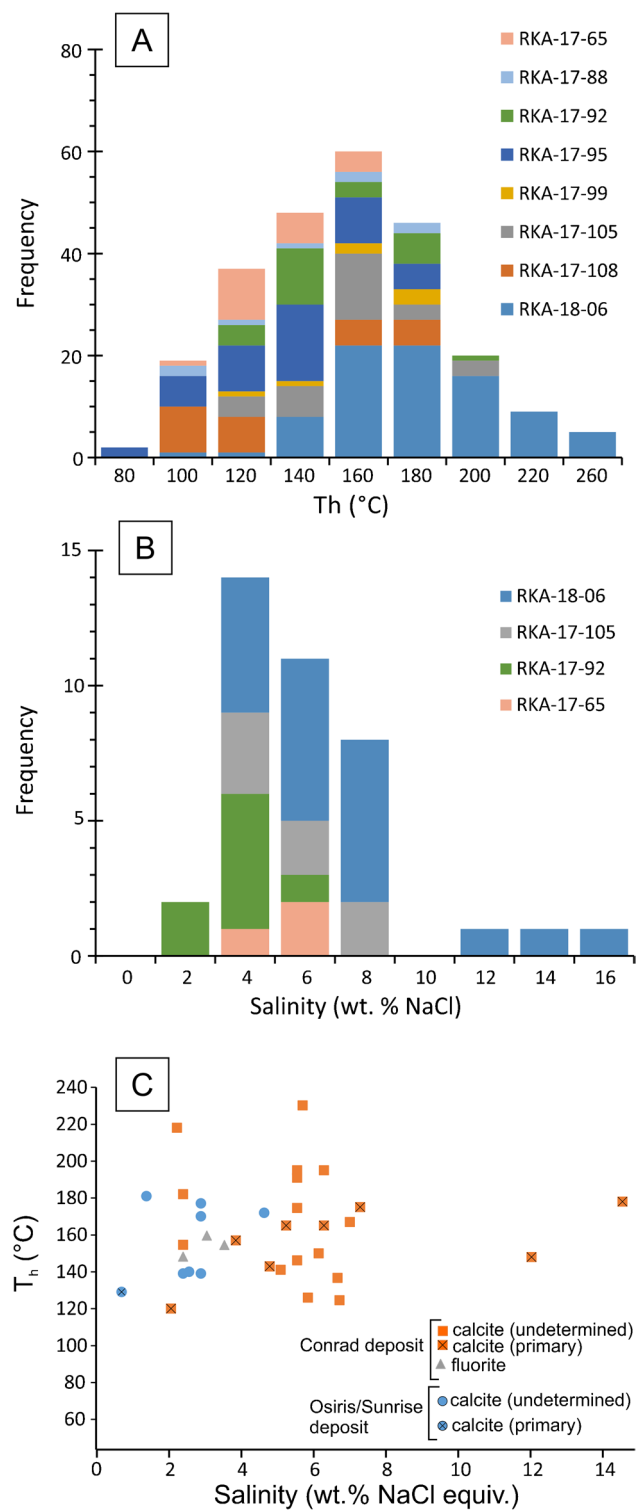


Fig. 4 Histograms of microthermometry results. **A** Homogenization temperatures (T_h) and **B** salinity calculated from ice melting using Bodnar (1993). **(C)** Plot of T_h vs salinity for fluid inclusions in calcite. Note that no clear trend is suggested by the data

dike, in agreement with the strong alteration of the dike (Pinet et al. 2022b). Finally, two samples from the Osiris/

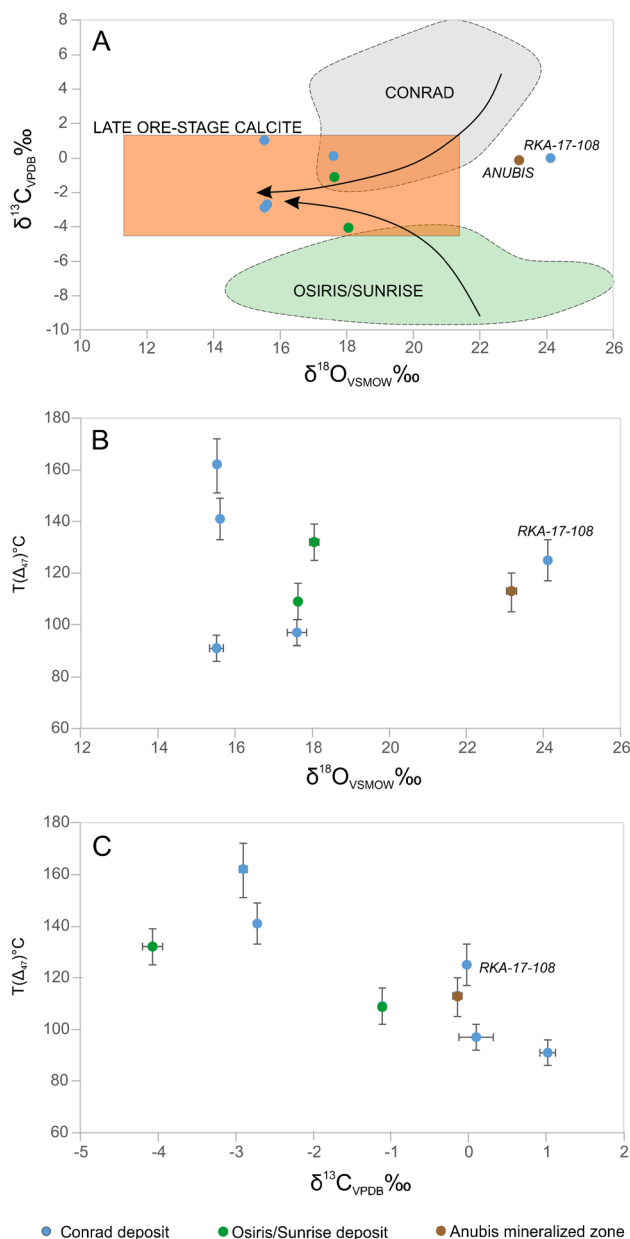


Fig. 5 Summary of clumped isotope results. **A** $\delta^{18}\text{O}_{\text{CaCO}_3}$ vs $\delta^{13}\text{C}$ diagram. The grey and green fields correspond to the isotopic values of the host rocks in the Conrad (data from Tucker 2015; Steiner and Hickey 2019; Pinet et al. 2022a) and Osiris/Sunrise deposits (data from Beaton 2015; Steiner and Hickey 2019; Pinet et al. 2022a), respectively. The orange box indicates the isotopic range of late ore-stage hydrothermal calcite for both the Conrad and Osiris/Sunrise deposits (data from Beaton 2015; Steiner and Hickey 2019; Pinet et al. 2022a). **B** Plot of $\delta^{18}\text{O}_{\text{CaCO}_3}$ vs $T(\Delta_{47})$ clumped isotope temperature. **C** Plot of $\delta^{13}\text{C}$ vs $T(\Delta_{47})$ clumped isotope temperature. Note that samples recording the higher temperatures have a depleted isotopic signature

Sunrise deposit yielded apparent temperatures $T(\Delta_{47})$ of 109 ± 7 and 132 ± 7 °C.

There are no clear trends between $\delta^{18}\text{O}_{\text{CaCO}_3}$ and $T(\Delta_{47})$ (Fig. 5B), and the three samples with the lowest $\delta^{18}\text{O}$

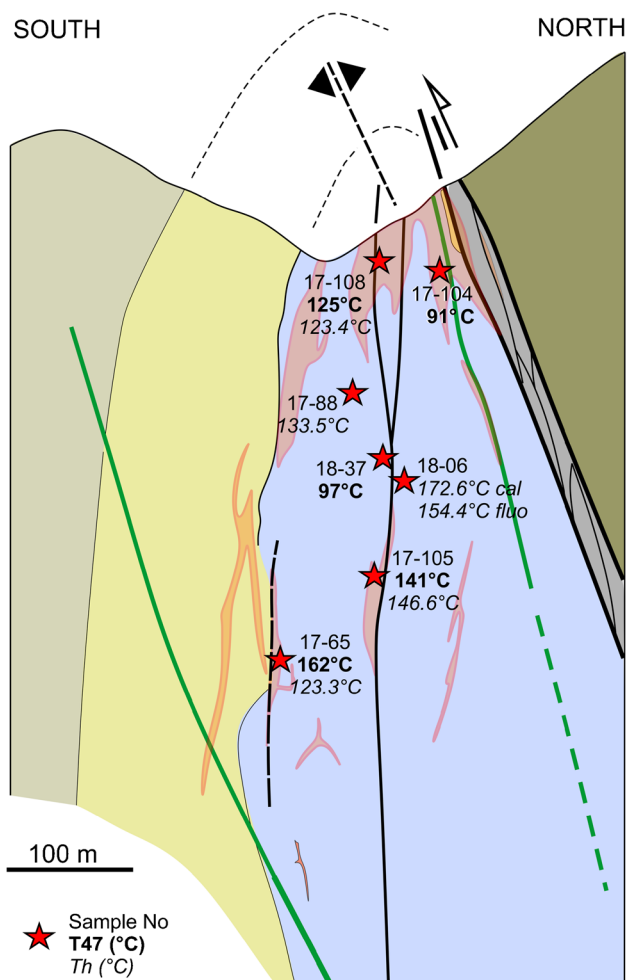


Fig. 6 Cross-section of the Conrad deposit with locations of samples analyzed for fluid inclusions and/or clumped isotopes. This section is parallel to the one shown in Fig. 1D and located 100 m to the west

(15.52–15.61‰) cover the whole range (91–162 °C) of $T(\Delta_{47})$. The distinction between “hot” and “warm” end-members is clearer on the $\delta^{13}\text{C}_{\text{CaCO}_3}$ vs $T(\Delta_{47})$ plot, in which higher temperature samples are characterized by more depleted carbon isotope values (Fig. 5C).

Apatite fission track

The two dated samples yielded overlapping AFT pooled ages of $49.2 + 5.6 / - 5.0$ and $44.2 + 9.2 / - 7.6$ Ma (ESM1, Table S3). For both samples, single AFT grain ages form a relatively narrow age population with no grain older than 225 Ma. This indicates that the samples have been completely annealed and experienced temperatures well in excess of 120 °C. Track lengths average 13.61 and 13.83 μm , with relatively narrow unimodal distribution.

Table 4 Summary of key findings and interpretations

Method	Key findings	Interpretation	Reference
Programed pyrolysis	Samples outside mineralized zones are over-mature	Regional maximum temperature > 150 °C	This study
Organic matter reflectance	Samples within or close (< 100 m) to Au-rich intervals experienced temperature of ca. 220 °C; Samples within Au-rich interval do not record higher temperatures than their immediate host rocks	Temperature of ca. 220 °C is either associated with regional burial or with hydrothermal fluid flow	This study
Petrographic observations	Pore filling pyrobitumen matured after emplacement, before mineralization	Hydrocarbon fluid did not transport gold	Pinet et al. 2022c
Fluid inclusions	Average homogenization temperatures between 123.3 and 172.6 °C; No significant variation of salinity (average 4.8%) with temperature	Temperature and salinity of late hydrothermal fluids	This study
Clumped isotopes	Temperature between 91 and 162 °C; Variation of the isotopic composition of fluids with temperature	Temperature of late hydrothermal fluids; Mixing of two fluids	This study
U–Pb	U–Pb zircon age (mineralized mafic dyke) and U–Pb in situ calcite ages (late ore calcites) overlap at ca. 74 Ma. Younger U–Pb ages on calcite postdate mineralization	Mineralization occurred at ca. 74 Ma	Pinet et al. 2022b
Apatite fission track	AFT data are compatible with the temperature of late hydrothermal fluids (derived from fluid inclusion and clumped isotopes) at 74 Ma	Continuous cooling after mineralization	This study

Discussion

The different thermal indicators used in this study each record only part of the geological history, yet direct comparison of these datasets requires caution (Table 4). Programed pyrolysis analyses and reflectance measurements provide information on the maximum temperature experienced by a given sample, which may or may not be associated with the Au-mineralizing event. For example, the fact that the lowest Bro value (2.35%) for borehole OS-12–130 corresponds to a high-grade sample (Fig. 2) suggests either that maximum thermal conditions are not related to Au-bearing fluids or that hydrothermal fluid flow was not restricted to mineralized intervals (i.e., that the thermal imprint of fluid flow varied only slightly for scales greater than the borehole length). Apatite fission track analyses are very sensitive to temperatures that characterize the partial annealing zone (~60–120 °C), but do not record the history at higher temperatures. Fluid inclusion microthermometry and clumped isotope analyses provide information on late ore-stage hydrothermal calcite and fluorite related to the mineralizing event at ca. 74 Ma. However, these data must be interpreted considering possible effects caused by younger event(s) unrelated to Au mineralization that may have led to the formation of secondary inclusions and to isotopic reordering.

Comparison between fluid inclusion and clumped isotope results

Both fluid inclusion microthermometric and clumped isotope data were generated for three samples from the Conrad deposit. LA–ICP–MS data presented in Pinet et al. (2022b) indicate that these three samples are characterized by a single calcite phase and by a simple systematic on the U–Pb Tera–Wasserburg plots, suggesting that they record a single hydrothermal event at ca. 74 Ma. Fluid inclusion mean T_h and clumped isotope data are within analytical error for samples RKA-17–108 and RKA-17–105, but there is a difference of ca. 39 °C for sample RKA-17–65. Post-formation processes are one possible explanation for the lower temperature recorded in fluid inclusions in sample RKA-17–65. Even if analysis of sample RKA-17–65 was carefully monitored, the lower T_h value compared to the $T(\Delta_{47})$ value may be due to inclusion necking or leaking after their formation. An alternative interpretation in which the clumped isotope temperature is overestimated due to solid-state diffusion of O and C atoms seems improbable, as there is no evidence that the sample experienced a high-temperature post-crystallization event. Comparison of fluid inclusion and clumped isotope datasets should also consider the difference in volume of the sample analyzed and the time frame

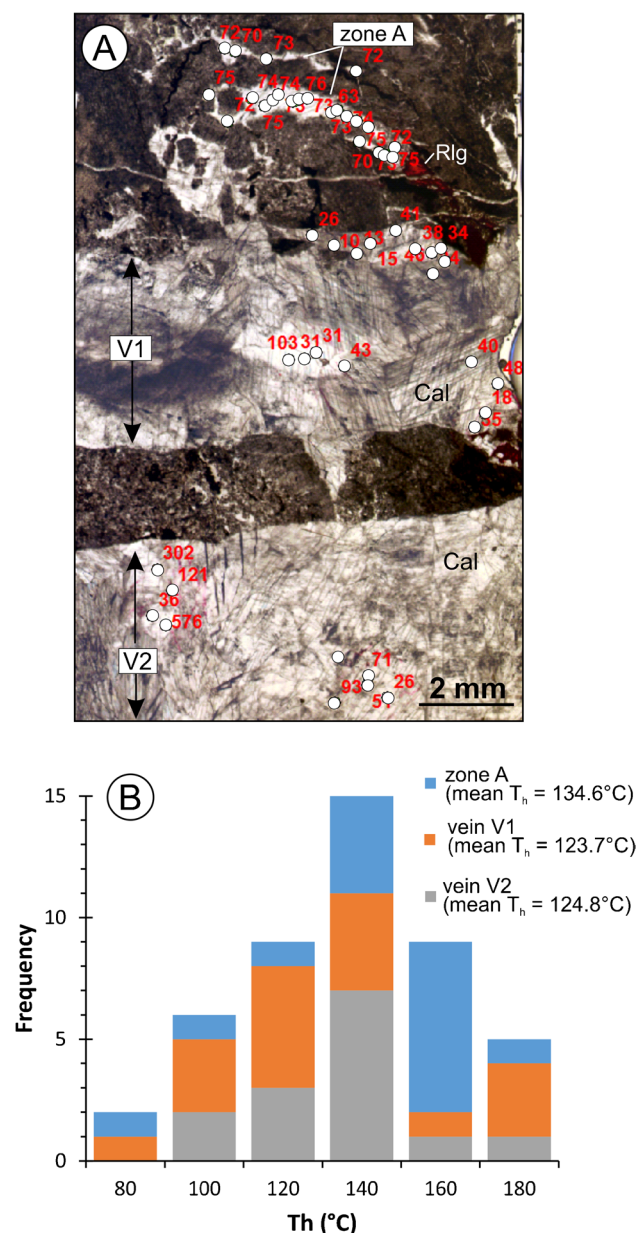


Fig. 7 Osiris sample RKA-17-95. **A** Thin section showing calcite in two parallel veins (V1 and V2) and in irregular-shaped zones (including zone A). Cal, calcite; Rlg, realgar. White dots correspond to LA-ICP-MS spot analyses (modified from Pinet et al. 2022b). **B** Histogram of fluid inclusion T_h in zone A and veins V1 and V2 (comments in the text)

of geological events. The clumped isotope data represent an “average” over a large crystal volume (possibly containing multiple generations of fluid inclusions), compared with measurements for individual 3- to 15- μm inclusion. This difference may mask variations in fluid temperature over short time periods in evolving hydrothermal systems. This interpretation is supported by the correspondence in mean T_h and $T(\Delta_{47})$ for two samples that have ranges in T_h of

118.5–182 °C (sample RKA-17-105) and 86.1–167.3 °C (sample RKA-17-108).

Variability of temperature estimates

The three samples with both fluid inclusion measurements and clumped isotope analyses are characterized by “simple” textures and geochemical zoning based on LA-ICP-MS elemental maps and in situ LA-ICP-MS calcite dating (Table 3). Clumped isotope temperatures $T(\Delta_{47})$ for these samples are 125–162 °C. These $T(\Delta_{47})$ values are consistent with the temperatures of 138 and 144 °C reported by Steiner et al. (2022) for UV-fluorescent veins. Two additional samples (RKA-18-24 and RKA-18-37) with “complex” or heterogeneous texture were also analyzed for clumped isotopes, LA-ICP-MS elemental mapping, and U–Pb dating. The $T(\Delta_{47})$ of 97 and 109 °C for these two samples is significantly lower compared with temperature estimates for “simple” samples. This discrepancy most likely reflects the effects of a post-crystallization hydrothermal event indicated by younger U–Pb ages.

Fluid inclusion T_h values on sample RKA-17-95 also provide some insights on homogenization temperature variability. Calcite in this sample occurs in 1) two parallel and well-defined, blocky calcite veins that are 0.8 and 3 cm wide (veins V1 and V2 in Fig. 7) and 2) in smaller and irregular-shaped veins (zone A in Fig. 7A). U–Pb spot analyses in zone A yielded robust overlapping ages of 72.2 ± 2.3 Ma age (see Fig. 6 in Pinet et al. 2022b). In contrast, some U–Pb ages in veins V1 and V2 are significantly younger than mineralization due to partly connected, thin (10 s of μm) microfractures that are significantly enriched in U (Pinet et al. 2022b). Fluid inclusion data for zone A record a mean T_h value of 134.6 ± 26.2 °C compared with values of 123.7 ± 29.5 and 124.8 ± 21.3 °C for veins V1 and V2, respectively (Fig. 7B). This ca. 10 °C difference in combination with the younger U–Pb ages supports a lower temperature post-crystallization thermal event.

Thermal history

Due to an absence of post-Permian rocks, the Mesozoic–Cenozoic history of the eastern Rackla belt is poorly constrained by geological evidence. However, information can be gained by inverse modeling of AFT data. The two AFT ages are not significantly different from the $47.0 + 8.6 / - 7.3$ Ma AFT age (based on an unknown number of grains) and a “single grain pooled age” of $37.4 + 7.4 / - 8.6$ Ma reported by Tucker (2015) for two samples collected within Au-bearing intervals from the Conrad deposit.

In this study, inverse models were performed using the HeFTy software (Ketchum 2013) taking into account a regional

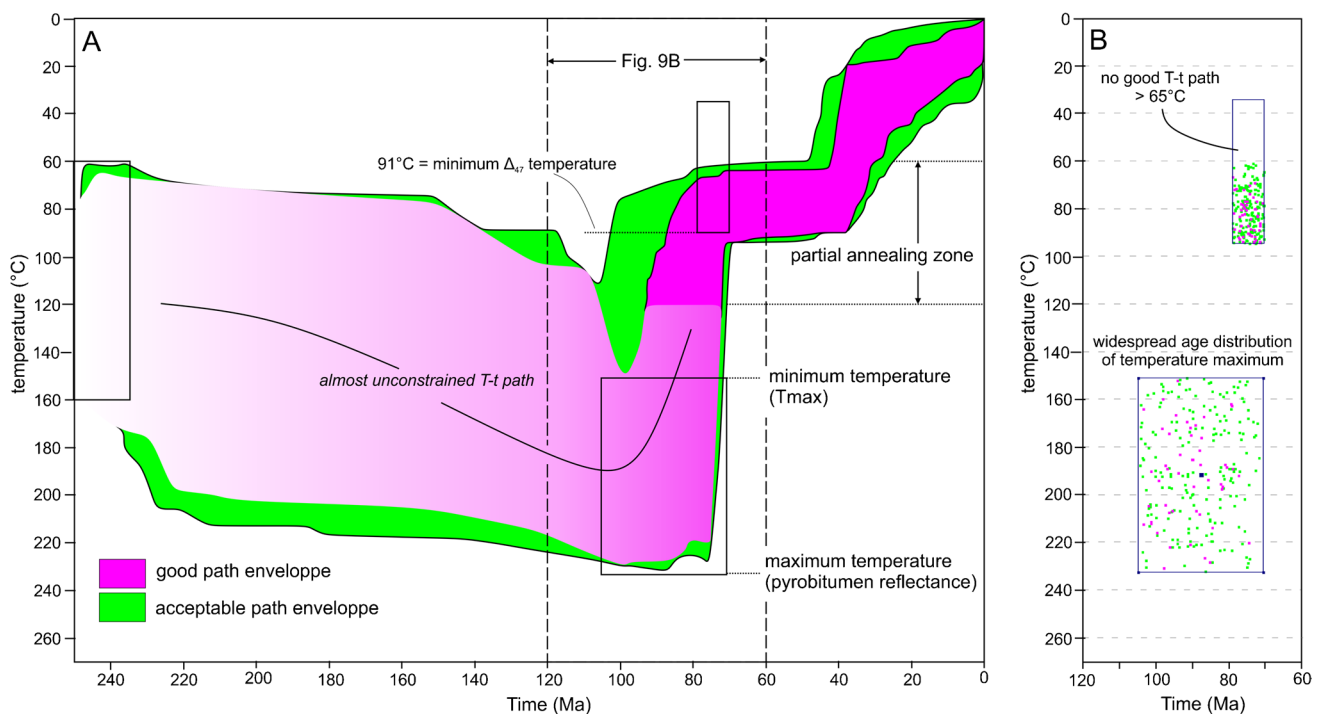


Fig. 8 **A** Inverse model result for sample 12-SI-058–1. The black boxes are geological constraints used during modeling. See ESM2 for modeling strategy. Note that modeling was done using two apatite populations characterized by a slightly different kinetic parameter, rnr0 . Modeling with a single apatite population yielded only “accept-

able” T-t paths. **B** Maximum temperatures experienced by the sample in each of the imposed T-t boxes. Magenta and green points correspond to the maximum temperatures of good and acceptable paths, respectively

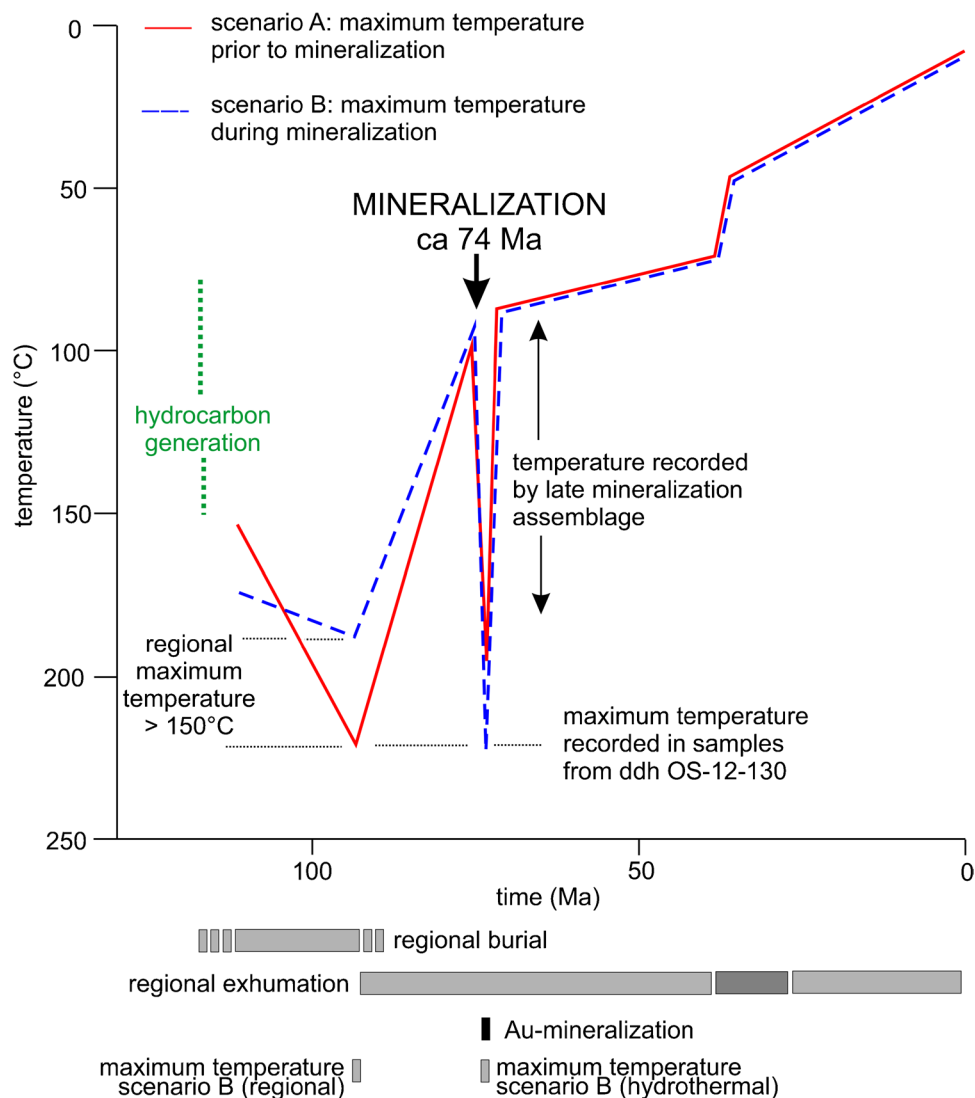
maximum temperature of $> 150\text{ }^{\circ}\text{C}$ based on programmed pyrolysis data for outcrop samples collected outside known mineralized zones that document overmature pyrobitumen. Among the parameters used during inverse modeling (see ESM2 for the detailed modeling strategy), the temperature constraint at ca. 74 Ma is clearly the most critical. We consider the lowest clumped isotope temperature ($91\text{ }^{\circ}\text{C}$) to represent a maximum temperature for the host rocks at ca. 74 Ma, because late ore-stage hydrothermal minerals (calcite, fluorite, and realgar) cannot have formed at temperatures lower than the host rocks.

Inverse modeling of sample 12-SI-058-1 indicates that the measured AFT age and fission-track length can be adequately fitted with a “simple” inverse model (Fig. 8). Similar results were obtained for sample 12-SI-054–2 even if apatite ages are more dispersed. Good T-t paths (i.e., with goodness-of-fit values of > 0.75 using Kuiper’s statistics) at 74 ± 4 Ma for sample 12-SI-058–1 are limited to temperatures between $91\text{ }^{\circ}\text{C}$, the lower temperature recorded by late hydrothermal calcite, and $65\text{ }^{\circ}\text{C}$, even if lower temperatures were allowed by the model (Fig. 8). This temperature range can be interpreted either as being associated with the waning stage of hydrothermal fluid flow or as the “regional” temperature of the host rock at 74 Ma. The envelope including all acceptable paths (i.e., with goodness of fit of > 0.05) is characterized by a marked decrease in temperature at ca. 35 Ma likely related to exhumation. Also,

the maximum temperature reached by the sample before 74 Ma spreads the whole range of temperatures allowed by the model between $150\text{ }^{\circ}\text{C}$ (attested by programmed pyrolysis data) and $220 \pm 10\text{ }^{\circ}\text{C}$ (attested by pyrobitumen reflectance). As AFT data do not record events that occurred at temperatures greater than the partial annealing zone, it is impossible to know whether samples experienced their maximum temperature in association with the building of the Cordillera, dike intrusion, and/or hydrothermal fluid flow.

Our two “preferred” T-t scenarios for Carlin-type gold deposits of central Yukon (Fig. 9) differ with respect to when rocks in borehole OS-12–130 experienced maximum temperatures ($\sim 220\text{ }^{\circ}\text{C}$). The maximum temperature in scenario A corresponds to regional maximum tectonic burial, whereas in scenario B it is related to local hydrothermal fluid flow. Whatever the scenario, hydrocarbon migration documented by pyrobitumen filling pores and fractures occurred during the sedimentary and/or tectonic burial of the sedimentary succession at temperature far below $200\text{ }^{\circ}\text{C}$, i.e., before Au mineralization. This timing agrees with petrographic observations suggesting that migrated hydrocarbon filling pores were matured after their emplacement (Fig. 10; Pinet et al. 2022c). Therefore, hydrocarbon-bearing-fluids did not transport Au at the deposit scale, an interpretation in agreement with the absence of hydrocarbons in fluid inclusions in the late-mineralization calcite and fluorite.

Fig. 9 Preferred T-t scenarios. The maximum temperature corresponds to maximum tectonic burial in scenario A, whereas maximum temperature is related to hydrothermal fluid flow in scenario B



Origin of fluids

Previous studies demonstrated that late ore-stage hydrothermal calcite has isotopic ratios distinct from unaltered host rocks and pre-ore veins in both the Conrad and Sunrise/Osiris deposits (Fig. 5A; Tucker 2015; Beaton 2015; Steiner and Hickey 2019; Pinet et al. 2022a; Steiner et al. 2022). Late ore-stage hydrothermal calcite is characterized by $\delta^{18}\text{O}$ (11.2–21.3‰ VSMOW) and $\delta^{13}\text{C}$ values (–4.5 to 1.3‰ VPDB) that are either lower (Conrad deposit) or higher (Sunrise and Osiris deposits) compared with surrounding rocks. The fact that samples of late ore-stage hydrothermal calcite have similar $\delta^{13}\text{C}$ values in the higher $\delta^{13}\text{C}$ Conrad and lower $\delta^{13}\text{C}$ Sunrise/Osiris limestones indicates similar fluid sources for each zone and limited carbon isotope exchange between late-ore hydrothermal fluids and the immediate host rocks on the mm–100 m scale (Pinet et al. 2022a; Steiner et al. 2022). Clumped

isotope data provide a means to study the evolution of fluids, because their $\delta^{18}\text{O}$ characteristics can be reconstructed using clumped and bulk isotopes of the carbonate that are measured simultaneously. The composition of the fluids in isotopic equilibrium with the vein calcite was calculated using the measured $T(\Delta_{47})$ and $\delta^{18}\text{O}$ values in conjunction with the calcite-water fractionation factors of Kim and O’Neil (1997) and Daëron et al. (2019). These data are presented in Fig. 11 and form a trend that indicates mixing between a higher-temperature end-member characterized by $\delta^{18}\text{O}_{\text{H}_2\text{O}} > 6\text{‰}$ and a lower-temperature end-member with $\delta^{18}\text{O}_{\text{H}_2\text{O}} < -2\text{‰}$ if using the fractionation of Kim and O’Neil (1997) (>4 and <–4‰ using the fractionation of Daëron et al. 2019). Sample RKA-17–108 represents a significant departure from this trend. Meteoric water, with $\delta^{18}\text{O}_{\text{H}_2\text{O}}$ values between –23 and –20‰ (VSMOW) for the latitude of central Yukon (Clark and Fritz 1997), is a potential candidate for the low temperature end-member.

However, the salinity of low homogenization temperature (T_h) fluid inclusions is not significantly different from the salinity of high T_h (Fig. 4C) inclusions, which is difficult to reconcile with an increased amount of meteoritic water in low-temperature hydrothermal fluids. Brines residing within fractures in tight rocks are another candidate for this low-temperature end-member, because their evolution over geological time scale under low temperature and low water–rock interactions is thought to promote a ^{18}O -depletion due to various degrees of isotope exchange with silica-rich rock, as recently documented in shield settings (Warr et al. 2021). Such brines could explain the presence of relatively high salinity yet ^{18}O depleted fluids for some of the samples. The origin of the high-temperature end-member fluid is difficult to ascertain as its $\delta^{18}\text{O}_{\text{H}_2\text{O}}$ value is close, or within the fields of magmatic, metamorphic, and, possibly, connate waters.

Comparison with Carlin-type deposits of Nevada

Carlin-type deposits of Nevada and Yukon share several characteristics, and the data give the opportunity to compare the thermal history for both regions (Table 1). In Carlin-type deposits of Nevada, fluid inclusions in jasperoid quartz at Jerritt Canyon (Hofstra 1994), Meikle (Lamb 1995), Carlin (Kuehn and Rose 1995), Turquoise Ridge (Shigehiro 1999), Getchell (Cline and Hofstra 2000), and Betze-Post (Lubben 2004; Lubben et al. 2012) deposits provide relatively consistent results. These studies indicate that ore-stage fluids had low to moderate temperatures (115–240 °C, mostly 160–220 °C), relatively low-salinity (0–10 wt.% NaCl eq, mostly < 6 wt%, but locally as high as 17 wt%), and they contained CO_2 (< 4 mol%) and low to trace amounts of H_2S and CH_4 (Cline et al. 2005; Muntean 2018). Evidence of boiling is generally lacking, with a possible exception reported by Groff (2019). A decrease in the fluid temperature at near constant salinity is recorded in fluid inclusions for late ore-stage minerals including fluorite (100–160 °C at Getchell, Cline, and Hofstra 2000), realgar (65–120 °C at Turquoise ridge; Groff 2020), and calcite (Carlin mine, mean $T_h = 141$ °C, Kuehn 1989; 137 °C, Groff et al. 2002; Getchellmine: $T_h = 100$ –140 °C, Cline and Hofstra 2000; Betze mine: mean $T_h = 166$ °C, Groff et al. 2002). The greater relative abundance of realgar in Au-rich zones in the Yukon deposits relative to most of those of Nevada led Pinet et al. (2022a) to hypothesize a slightly lower temperature of formation for the Yukon deposits. However, the temperature estimates for the late ore-stage minerals in deposits of Nevada are not significantly different from those obtained in Yukon (Table 1), suggesting that Carlin-type deposits of Nevada and Yukon formed at similar temperatures.

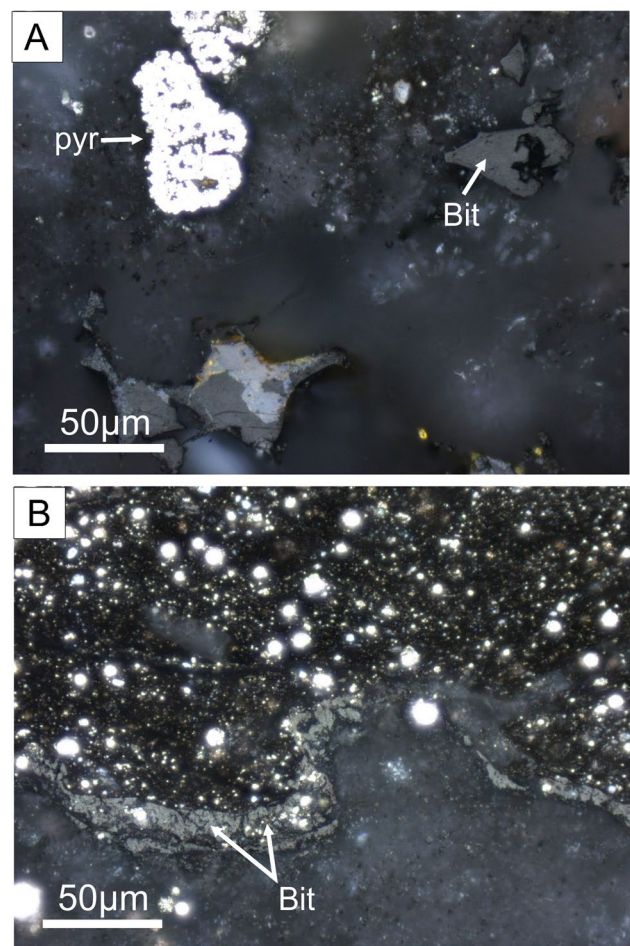
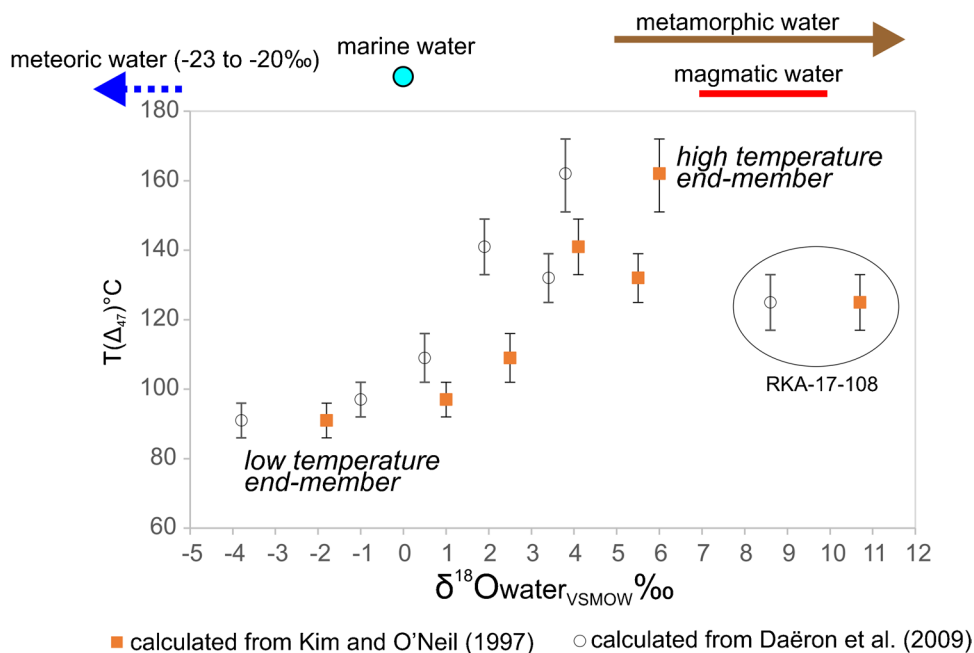


Fig. 10 Organic petrography photomicrographs taken by incident white light with oil immersion $\times 50$ objective. **A** Accumulation of fused fine crystalline pyrite (pyr) in the host rock. Pores within the host rock filled with pyrobitumen (pyr); borehole OS-12-130; 237.2 m. **B** Boundary between organic-rich shale and host rock with pyrobitumen that accumulated mainly at the boundary (borehole OS-12-130; 190.7 m)

Conclusion

Several techniques were used to investigate the thermal framework of Au-bearing Carlin-type deposits in central Yukon and better understand the evolution of such class of ore deposit. The T_{max} parameter derived from programmed pyrolysis analyses indicates that organic matter is overmature and records temperatures of > 150 °C regionally. Temperature of crystallization of the late-ore mineral assemblage associated with the waning stage of the mineralization event at ca. 74 Ma has been investigated through fluid inclusion analyses and clumped isotope measurements. Among the three samples with both fluid inclusion and clumped isotope analyses, two yielded similar temperature estimates, whereas one has a significantly lower fluid inclusion temperature. Data also indicate that samples previously identified as

Fig. 11 Plot of $\delta^{18}\text{O}_{\text{H}_2\text{O}}$ vs $T(\Delta_{47})$. At the top of the plot are $\delta^{18}\text{O}$ values for various types of water (Clark and Fritz 1997; Bierlein and Crowe 2000)



“complex” or texturally and geochemically heterogeneous have lower temperature estimates, suggesting that calcite locally records post-mineralization processes. Mean fluid inclusion T_h in eight samples range from 123.3 to 172.6 °C, with a mean calculated salinity of 4.8% NaCl equiv. These values are comparable to clumped isotope temperatures obtained for eight calcite samples ranging from 91 to 162 °C. Calculation of the composition of the fluid in equilibrium with calcite during crystallization supports mixing of two fluids of variable temperature and isotopic signature, the higher temperature end-member being characterized by higher $\delta^{18}\text{O}_{\text{H}_2\text{O}}$ values. In thermal scenarios based on T_{max} , fluid inclusion analysis, clumped isotope measurements, and apatite fission track modeling, the ca. 220 °C temperature estimated through pyrobitumen reflectance measurements is either related to maximum tectonic burial prior to gold mineralization or to the early stages of the Au-bearing hydrothermal event.

This study demonstrates the benefit of using different analytical techniques, as each method brings some information on the temperature evolution of Au-mineralized zones and/or their host rocks. Although underutilized, organic matter geothermometers (programed pyrolysis data and reflectance measurements) provide robust and relatively inexpensive temperature constraints both on the regional and deposit scales for deposits hosted in sedimentary rocks. Comparison of fluid inclusions and clumped isotopes (Δ_{47}) results in various settings and, on different scales, will likely generate new insights on hydrothermal fluid temperature variations in space and time. Moreover, clumped isotopes (Δ_{47}) in lower temperature and younger Carlin-type deposits are shown to yield accurate temperature estimates compared to Archean

orogenic gold deposits where reordering of isotopic bounds over time has obliterated the higher temperature of formation (Quesnel et al. 2022).

Supplementary Information The online version contains supplementary material available at <https://doi.org/10.1007/s00126-023-01162-2>.

Acknowledgements We sincerely thank ATAC Resources for logistical and scientific support. Jean-Luc Pilote reviewed an early version of the manuscript. Maurice Colpron (YGS) is warmly acknowledged for discussion and for providing the results of AFT analyses. Formal review by J. Groff and H. Frimmel helped to clarify the manuscript. This work is part of the Natural Resources Canada’s Targeted Geoscience Initiative and is Geological Survey of Canada contribution number 20220218 and Yukon Geological Survey contribution number 061.

Author contribution All authors contributed to the study conception and design. Sample collection was done by Nicolas Pinet and Patrick Sack. Sample preparation and analysis were performed by Omid Haeri-Ardakani and Josué Jautzy. The first draft of the manuscript was written by Nicolas Pinet, and all authors commented on previous versions of the manuscripts. All authors read and approved the final version of the manuscript.

Funding Open access funding provided by Natural Resources Canada.

Declarations

Conflict of interest The authors declare no competing interests.

Open Access This article is licensed under a Creative Commons Attribution 4.0 International License, which permits use, sharing, adaptation, distribution and reproduction in any medium or format, as long as you give appropriate credit to the original author(s) and the source, provide a link to the Creative Commons licence, and indicate if changes were made. The images or other third party material in this article are included in the article’s Creative Commons licence, unless indicated otherwise in a credit line to the material. If material is not included in the article’s Creative Commons licence and your intended use is not

permitted by statutory regulation or exceeds the permitted use, you will need to obtain permission directly from the copyright holder. To view a copy of this licence, visit <http://creativecommons.org/licenses/by/4.0/>.

References

- Anderson NT, Kelson JR, Kele S, Daëron M, Bonifacie M, Horita J et al (2021) A unified clumped isotope thermometer calibration (0.5–1,100°C) using carbonate-based standardization. *Geophys Res Lett* 48:e2020GL092069. <https://doi.org/10.1029/2020GL092069>
- Arehart GB, Chakurian AM, Tretbar DR, Christensen JN, McInnes BA, Donelick RA (2003) Evaluation of radioisotope dating of Carlin-type deposits in the Great Basin, western North America, and implications for deposit genesis. *Econ Geol* 98:235–248
- Arehart GB, Ressel M, Carne R, Muntean J (2013) A comparison of Carlin-type deposits in Nevada and Yukon. *Soc Econ Geol Spec Publ* 17:389–401
- ASTM (2014) Standard test method for microscopical determination of the reflectance of vitrinite dispersed in sedimentary rocks, D7708-14. astm.org/catalog/search/results?q=D7708
- Barker CE, Pawlewicz MJ (1994) Calculation of vitrinite reflectance from thermal histories and peak temperatures. In: *Vitrinite reflectance as a maturity parameter*. Am Chem Soc Symp Ser 570(Chapter 14):216–229
- Barker SLL, Hickey KA, Cline JS, Dipple GM, Kilburn MR, Vaughan JR, Longo AA (2009) Uncloaking invisible gold: use of nanoSIMS to evaluate gold, trace elements, and sulfur isotopes in pyrite from Carlin-type gold deposits. *Econ Geol* 104:897–904
- Beaton NI (2015) Diagenetic controls on hydrothermal fluid flow in the Osiris, Isis and Isis East Carlin-type showings, Nadaleen trend, Yukon. M.Sc. thesis, Edmonton, Canada, The University of Alberta, 180 p.
- Bernasconi SM, Hu B, Wacker U, Fiebig J, Breitenbach SFM, Rutz T (2013) Background effects on Faraday collectors in gas-source mass spectrometry and implications for clumped isotope measurements. *Rapid Commun Mass Spectrom* 27:603–612
- Bernasconi SM, Daëron M, Bergmann KD, Bonifacie M, Meckler AN, Affek HP et al (2021) InterCarb: a community effort to improve interlaboratory standardization of the carbonate clumped isotope thermometer using carbonate standards. *Geochim Geophys Geosyst* 22:e2020GC009588. <https://doi.org/10.1029/2020GC009588>
- Beysac O, Goffé B, Chopin C, Rouzaud N (2002) Raman spectra of carbonaceous material in metasediments: a new geothermometer. *J Metamorph Geol* 20:859–871
- Bierlein FP, Crowe DF (2000) Phanerozoic orogenic lode gold deposits. *SEG Rev* 13:103–139
- Bodnar RJ (1993) Revised equation and table for determining the freezing point depression of H₂O-NaCl solutions. *Geochim Cosmochim Acta* 57:683–684
- Brand WA, Assonov SS, Coplen TB (2010) Correction for the ¹⁷O interference in $\delta^{13}\text{C}$ measurements when analyzing CO₂ with stable isotope mass spectrometry (IUPAC Technical Report). *Pure Appl Chem* 82:1719–1733
- Burman J, Gustafsson O, Segl M, Schmitz B (2005) A simplified method of preparing phosphoric acid for stable isotope analyses of carbonates. *Rapid Commun Mass Spectrom* 19:3086–3088
- Clark ID, Fritz P (1997) *Environmental isotopes in hydrogeology*. CRC Press, Boca Raton, 342 p. <https://doi.org/10.1201/9781482242911>.
- Cline JS, Hofstra AA (2000) Ore-fluid evolution at the Getchell Carlin-type gold deposit, Nevada, USA. *Eur J Mineral* 12:195–212
- Cline JS, Hofstra AH, Muntean JL, Tosdal RM, Hickey KA (2005) Carlin-type gold deposits in Nevada: critical geologic characteristics and viable models. *Econ Geol* 100:451–484
- Colpron M., Moynihan D, Israel S, Abbott G (2013). Geologic map of the Rackla belt, east-central Yukon (NTS 106C/1–4, 106D/1). Yukon Geological Survey, Open File 2013–13, scale 1:50 000.
- Cook HE (2015) The evolution and relationship of the western North American Paleozoic carbonate platform and basin depositional environments to Carlin-type gold deposits in the context of carbonate sequence stratigraphy. In: Pennell WM, Garside LJ (eds) *New concepts and discoveries: Geological Society of Nevada 2015 Symposium proceedings*. Geological Society of Nevada, Reno, Nevada, pp 1–80
- Daëron M, Blamart D, Peral M, Affek HP (2016) Absolute isotopic abundance ratios and the accuracy of $\Delta 47$ measurements. *Chem Geol* 442:83–96
- Daëron M, Drysdale RN, Peral M, Huyghe D, Blamart D, Coplen TB, Lartaud F, Zanchetta G (2019) Most Earth-surface calcites precipitate out of isotopic equilibrium. *Nat Commun* 10:1–7
- de Almeida CM, Ribeiro Olivo G, Chouinard A, Weakly C, Poirier G (2010) Mineral paragenesis, alteration, and geochemistry of the two types of gold ore and the host rocks from the Carlin-type deposits in the southern part of the Goldstrike property, northern Nevada: implications for sources of ore-forming elements, ore genesis, and mineral exploration. *Econ Geol* 105:971–1004
- Donelick RA, O’Sullivan PB, Ketcham RA (2005) Apatite fission-track analysis. *Rev Mineral Geochem* 58:49–94
- Eiler JM (2007) ‘Clumped-isotope’ geochemistry: the study of naturally-occurring, multi-substituted isotopologues. *Earth Planet Sci Lett* 262:309–327
- Eiler JM (2013) The isotopic anatomies of molecules and minerals. *Annu Rev Earth Planet Sci* 41:411–441
- Fall A, Bodnar RJ (2018) How precisely can the temperature of a fluid event be constrained using fluid inclusion? *Econ Geol* 113:1817–1843
- Gabrielse H (1967) Tectonic evolution of the northern Canadian Cordillera. *Can J Earth Sci* 4:271–298
- Goldstein RH (2003) Petrographic analysis of fluid inclusions. In: Samson, I., Anderson, A., Marshall, D. (Eds.), *Fluid Inclusions Analysis and Interpretation*. Mineralogical Association of Canada Short Course Series, vol. 32, pp. 9–53.
- Goldstein RH (2012) Fluid inclusion geothermometry in sedimentary systems: from paleoclimate to hydrothermal. In N. B. Harris & K. E. Peters (Eds.), *Analyzing the Thermal History of Sedimentary Basins: Methods and Case Studies* (Issue 103, pp. 45–63). SEPM (Society for Sedimentary Geology). <https://doi.org/10.2110/sepm.103.045>
- Grady SP, Anderson RG (1993) Evolution of the northern Cordilleran miogeocline, Nahanni map area (1051), Yukon and Northwest Territories. *Geol Surv Can Mem* 428:214
- Grauch VJS, Rodriguez BD, Wooden JL (2003) Geophysical and isotopic constraints on crustal structure related to mineral trends in north-central Nevada and implications for tectonic history. *Econ Geol* 98:269–286
- Groff JA (2018) Fluid mixing during late-stage Carlin-type mineralization in the Getchell and Twin Creeks deposits, Nevada. *Ore Geol Rev* 101:960–965
- Groff JA (2019) Evidence of boiling and epithermal vein mineralization in Carlin-type deposits on the Getchell trend, Nevada. *Ore Geol Rev* 106:340–350
- Groff JA (2020) Genetic implications of regional vs. fracture-controlled fluid flow in Carlin-type gold deposits, Nevada. *Ore Geol Rev* 117:103282

- Groff JA, Campbell AR, Norman DI (2002) An evaluation of fluid inclusion microthermometric data for orpiment-realgar-calcite-barite-gold mineralization at the Betze and Carlin mines, Nevada. *Econ Geol* 97:1341–1346
- Hartkopf-Fröder C, Königshof P, Littke R, Schwarzbauer J (2015) Optical thermal maturity parameters and organic geochemical alteration at low grade diagenesis to anchimetamorphism: a review. *Int J Coal Geol* 150–151:74–119
- He B, Olack GA, Colman AS (2012) Pressure baseline correction and high-precision CO₂ clumped-isotope (δ^{47}) measurements in bellows and micro-volume modes. *Rapid Commun Mass Spectrom* 26:2837–2853
- Hofstra AH (1994) Geology and genesis of the Carlin-type gold deposits in the Jerritt Canyon district, Nevada. Ph.D thesis, Boulder, USA, University of Colorado, 719 p.
- Jarvie DM, Hill RJ, Ruble TE, Pollastro RM (2007) Unconventional shale-gas systems: the Mississippian Barnett Shale of north-central Texas as one model for thermogenic shale-gas assessment. *Am Assoc Pet Geol Bull* 91:475–499
- Jautzy JJ, Savard MM, Dhillon RS, Bernasconi SM, Smirnov A (2020) Clumped isotope temperature calibration for calcite: bridging theory and experimentation. *Geochem Perspect Lett* 14:36–41
- John CM, Bowen D (2016) Community software for challenging isotope analysis: First applications of ‘Easotope’ to clumped isotopes. *Rapid Commun Mass Spectrom* 30:2285–2300
- Ketcham RA (2005) Forward and inverse modeling of low-temperature thermochronometry data. *Rev Mineral Geochem* 58:275–314
- Ketcham RA (2013) HeFTy, version 1.8.2. Manual user dated 2 october 2013.
- Kim ST, O’Neil JR (1997) Equilibrium and nonequilibrium oxygen isotope effects in synthetic carbonates. *GeochimicaCosmochimica Acta* 61:3461–3475
- Kuehn CA (1989) Studies of disseminated gold deposits near Carlin, Nevada: evidence for a deep geologic setting of ore formation: Unpub. PhD thesis, Univ. Park, Pennsylvania State Univ., 386p.
- Kuehn CA, Rose AW (1995) Carlin gold deposits, Nevada: origin in a deep zone of mixing between normally pressured and overpressured fluids. *Econ Geology* 90:17–36
- Lafargue E, Marquis F, Pillot D (1998) Rock-Eval 6 applications in hydrocarbon exploration, production, and soil contamination studies. *Rev Inst fr pétrol* 53:421–437
- Lamb JB (1995) A petrographic and fluid inclusion study of the Purple vein and Post/Betze orebodies, Carlin, Nevada. Master Thesis, Univ. Nevada, Las Vegas, p 161
- Landis CR, Castaño JR (1995) Maturation and bulk chemical properties of a suite of solid hydrocarbons. *Org Geochem* 22:137–149
- Lindgren W (1933) Mineral deposits, 4th edn. McGraw-Hill, New York, p 930
- Lovering TG (1972) Jasperoid in the United States: its characteristics, origin and economic significance. *U S Geol Surv Prof pap* 710:164
- Lubben JD (2004) Silicification across the Betze-Post Carlin-type Au deposit: clues to ore fluid properties and sources, northern Carlin trend, Nevada. Master thesis, Univ. of Nevada, Las Vegas, 156 pp.
- Lubben JD, Cline JS, Barker SLL (2012) Ore fluid properties and source from quartz-associated gold at the Betze-Post Carlyn-type gold deposit, Nevada, United States. *Econ Geol* 107:1351–1385
- Malusà MG, Fitzgerald PG (2018) Fission-track thermochronology and its application to geology. Springer, 393 p.
- Meckler AN, Ziegler M, Millán MI, Breitenbach SFM, Bernasconi SM (2014) Long-term performance of the Kiel carbonate device with a new correction scheme for clumped isotope measurements. *Rapid Commun Mass Spectrom* 28:1705–1715
- Moynihan D (2016) Bedrock geology compilation of the eastern Rackla belt, NTS 105N/15, 105N/16, 105O/13, 106B/4, 106C/1, 106C/2, east-central Yukon. Yukon Geological Survey, Open File 2016–2, scale 1:75 000.
- Moynihan D, Strauss JV, Padget CD, Nelson LL (2019) Upper Windermere Supergroup and the transition from rifting to continent-margin sedimentation, Nadaleen River area, northern Canadian Cordillera. *Geol Soc Am Bull* 131:1673–1701
- Müller IA, Fernandez A, Radke J, van Dijk J, Bowen D, Schwieters J, Bernasconi SM (2017) Carbonate clumped isotope analyses with the long-integration dual-inlet (LIDI) workflow: scratching at the lower sample weight boundaries. *Rapid Commun Mass Spectrom* 31:1057–1066
- Muntean JL, Cline JS, Simon AC, Longo AA (2011) Magmatic-hydrothermal origin of Nevada’s Carlin-type gold deposits. *Nat Geosciences* 4:122–127
- Muntean J (2018) The Carlin gold system: applications to exploration in Nevada and beyond. In Muntean, J. (ed.) *Diversity of Carlin-Style Gold Deposits: Society of Economic Geologists, Reviews in Economic Geology* 20, pp. 39–88.
- Petersen SV, Defliese WF, Saenger C, Daëron M, Huntington KW, John CM et al (2019) Effects of improved ¹⁷O correction on interlaboratory agreement in clumped isotope calibrations, estimates of mineral-specific offsets, and temperature dependence of acid digestion fractionation. *Geochem Geophys Geosyst* 20:3495–3519. <https://doi.org/10.1029/2018GC008127>
- Pinet N, Sack P (2019) Macroscopic control on Carlin-type gold mineralization in north-central Yukon, in Rogers, N., ed., *Targeted Geoscience Initiative: 2018 Report of Activities: Geological Survey of Canada*. Open File 8549:89–103
- Pinet N, Sack P, Mercier-Langevin P, Davis WJ, Petts DC, Lavoie D, Percival JB, Dubé B, Colpron M, Haeri-Ardakani O, Brake VI (2022) Yukon’s Carlin-type gold deposits (Rackla belt, Canada): main characteristics and new insights on alteration styles and geochemistry. *Econ Geol* 117:875–904
- Pinet N, Davis WE, Petts DC, Sack P, Mercier-Langevin P, Lavoie D, Jackson SJ (2022) U-Pb vein calcite dating reveals the age of Carlin-type gold deposits of central Yukon, and a contemporaneity with a regional intrusion-related metallogenic event. *Econ Geol* 117:905–922
- Pinet N, Haeri-Ardakani O, Cesar J, Petts D, Debuhr C, Sack P (2022) Exploring the link between organic matter and Carlin-type gold mineralization: new insights from Yukon deposits. *Geol Surv Can Open File* 8895:22
- Pinet N, Brake V (2018) Preliminary compilation of apatite fission-track data in Geological Survey of Canada. Open File 8454, 1 poster.
- Pinet, N., Sack, P., Mercier-Langevin, P., Colpron, M., Lavoie, D., Dubé, B., Brake, V.I. (2020a) Neoproterozoic-hosted Carlin-type mineralization in central Yukon, part 1: regional- to prospect-scale geological controls: in Mercier-Langevin, P., Lawley, C.J.M., and Castonguay, S, eds., *Targeted Geoscience Initiative 5: Contributions to the Understanding of Gold Systems: Geological Survey of Canada*, Open File 8712, p. 281–297.
- Pinet, N., Sack, P., Mercier-Langevin, P., Davis, W.E., Lavoie, D., Haeri-Ardakani, O., Dubé, B., Cline, J., Petts, D., Jautzy, J., Jackson, S.E., Percival, J.B., Savard, M.M., Brake, V.I. (2020b) Neoproterozoic-hosted Carlin-type mineralization in central Yukon, part 2: mineralization, in Mercier-Langevin, P., Lawley, C.J.M., and Castonguay, S, eds., *Targeted Geoscience Initiative 5: Contributions to the Understanding of Gold Systems: Geological Survey of Canada*, Open File 8712, p. 299–314.
- Quesnel B, Jautzy J, Scheffer C, Raymond G, Beaudoin G, Jorgensen T, Pinet N (2022) Clumped isotope geothermometry in old mesothermal hydrothermal systems (Archean Augmitto-Bouzan orogenic gold deposits, Abitibi, Québec, Canada): a note of caution and a look forward. *Chem Geol* 610:121099

- Ressel MW, Henry CD (2006) Igneous geology of the Carlin trend, Nevada: development of the Eocene plutonic complex and significance for Carlin-type gold deposits. *Econ Geol* 101:347–383
- Rhys D, Valli F, Burgess R, Heitt D, Griesel G, Hart K (2015) Controls of fault and fold geometry on the distribution of gold mineralization on the Carlin trend. *Geological Society of Nevada, New Concepts and Discoveries: 2015 Symposium Proceedings*, p. 333–389.
- Ridley J (2013) *Ore deposit geology*. Cambridge University Press, Cambridge, p 409
- Ristorcelli S, Ronning P, Martin C, Christensen O (2018) Technical report and estimate of mineral resources for the Osiris project, Yukon, Canada (https://www.atacresources.com/assets/img/Osiris_Resource_Estimate_and_Technical_Report_2018.pdf)
- Roedder E (1984) Fluid inclusions. *Rev Mineral Mineral Soc Am* 12:646
- Sack P, Cline J, Ren M, Petts D, Pinet N (2019) Gold bearing pyrite in Carlin-type gold prospects of the Nadaleen trend, Yukon [abs.]. Geological Association of Canada annual meeting, Quebec, Canada, p. 169.
- Schauer AJ, Kelson J, Saenger C, Huntington KW (2016) Choice of ^{17}O correction affects clumped isotope (Δ_{47}) values of CO_2 measured with mass spectrometry. *Rapid Commun Mass Spectrom* 30:2607–2616
- Schmid TW, Bernasconi SM (2010) An automated method for ‘clumped-isotope’ measurements on small carbonate samples. *Rapid Commun Mass Spectrom* 24:1955–1963
- Shigehiro M (1999) Mineral paragenesis and ore fluids at the Turquoise Ridge gold deposit, Nevada. Master thesis, Univ. Nevada, Las Vegas, p 152
- Steiner AP, Hickey KA, Huntington KW, Schauer AJ (2022) ‘Roll-front’ mass transfer of carbonate cations in Carlin-type gold deposits: insights from UV-fluorescent calcite veins. *Econ Geol* 117:1225–1249
- Steiner AP, Hickey KA (2019) Ore-stage calcite vein in the Carlin-type Au deposits of the Nadaleen trend, Yukon: a new addition to the geologist’s tool-kit, Proceedings of the 15th SGA biennial meeting, Glasgow, August 2019, 4 p.
- Steiner AP, Hickey KA, Coulter A (2018) The structural framework for Carlin-type gold mineralization in the Nadaleen trend, Yukon. In MacFarlane, K.E.(ed.) *Yukon Exploration and Geology 2017*, Yukon Geological Survey, p. 139–149.
- Timmons JM, Karlstrom KE, Dehler CM, Eissman JW, Heizler MT (2001) Proterozoic multistage (ca. 1.1 and 0.8 Ga) extension recorded in the Grand Canyon Supergroup and establishment of northwest- and north-trending tectonic grains in the southwestern United States. *Geol Soc Am Bull* 113:163–190
- Tissot BP, Welte DH (1984) *Petroleum formation and occurrence*, 2nd edn. Springer-Verlag, Berlin, p 699
- Tucker MJ (2015) *Geology, mineralization and geochronology of the Conrad zone Carlin-type prospect, east-central Yukon Territory, Canada*. Master thesis, Vancouver, Canada, The University of British Columbia, 160 p.
- Tucker MJ, Lane JC, Hart CJR (2018) Overview of Carlin-type prospects of the Nadaleen trend: a Yukon analogue to Carlin-type gold mineralization of the Great Basin, in Muntean, J., ed., *Diversity of Carlin-style gold deposits*. *Soc Econ Geol Rev Econ Geol* 20:235–256
- Warr O, Giunta T, Onstott TC, Kieft TL, Harris RL, Nisson DM, Sherwood Lollar B (2021) The role of low-temperature ^{18}O exchange in the isotopic evolution of deep subsurface fluids. *Chem Geol* 561:120027
- Wilkinson JJ (2001) Fluid inclusions in hydrothermal ore deposits. *Lithos* 55:229–272

Publisher’s note Springer Nature remains neutral with regard to jurisdictional claims in published maps and institutional affiliations.